

1 **Beijing Climate Center Earth System Model version 1 (BCC-ESM1):**

2 **Model Description and Evaluation of Aerosol Simulations**

3  
4 **Tongwen Wu<sup>1\*</sup>, Fang Zhang<sup>1</sup>, Jie Zhang<sup>1</sup>, Weihua Jie<sup>1</sup>, Yanwu Zhang<sup>1</sup>, Fanghua Wu<sup>1</sup>,**  
5 **Laurent Li<sup>1,2</sup>, Jinghui Yan<sup>1</sup>, Xiaohong Liu<sup>3</sup>, Xiao Lu<sup>4</sup>, Haiyue Tan<sup>4</sup>, Lin Zhang<sup>4</sup>,**  
6 **Jun Wang<sup>5</sup>, Aixue Hu<sup>6</sup>**

7  
8 <sup>1</sup>Beijing Climate Center, China Meteorological Administration, Beijing, China

9 <sup>2</sup>Laboratoire de M é t é o r o l o g i e D y n a m i q u e, I P S L, C N R S, S o r b o n n e U n i v e r s i t é E c o l e N o r m a l e  
10 S u p é r i e u r e, E c o l e P o l y t e c h n i q u e, P a r i s, F r a n c e

11 <sup>3</sup>Texas A&M University, College Station, TX, USA

12 <sup>4</sup>Laboratory for Climate and Ocean-Atmosphere Studies, Department of Atmospheric and  
13 Oceanic Sciences, School of Physics, Peking University, Beijing, China

14 <sup>5</sup>University of Iowa, Iowa City, IA 52242, USA

15 <sup>6</sup>National Center for Atmospheric Research, PO Box 3000, Boulder, Colorado 80307-3000,  
16 USA

17  
18  
19  
20 *Correspondence to:* Tongwen Wu ([twwu@cma.gov.cn](mailto:twwu@cma.gov.cn))

21  
22 Submit to Geosci. Model Dev.  
23  
24

25 **Abstract.** BCC-ESM1 is the first version of a fully-coupled Earth System Model with  
26 interactive atmospheric chemistry and aerosols developed by the Beijing Climate Center,  
27 China Meteorological Administration. Major aerosol species (including sulfate, organic  
28 carbon, black carbon, dust and sea salt) and greenhouse gases are interactively simulated with  
29 a whole panoply of processes controlling emission, transport, gas-phase chemical reactions,  
30 secondary aerosol formation, gravitational settling, dry deposition, and wet scavenging by  
31 clouds and precipitation. Effects of aerosols on radiation, cloud, and precipitation are fully  
32 treated. The performance of BCC-ESM1 in simulating aerosols and their optical properties is  
33 comprehensively evaluated as required by the Aerosol Chemistry Model Intercomparison  
34 Project (AerChemMIP), covering the preindustrial mean state and time evolution from 1850  
35 to 2014. The simulated aerosols from BCC-ESM1 are quite coherent with  
36 CMIP5-recommended data, in-situ measurements from surface networks (such as IMPROVE  
37 in the U.S. and EMEP in Europe), and aircraft observations. A comparison of modeled  
38 aerosol optical depth (AOD) at 550 nm with satellite observations retrieved from Moderate  
39 Resolution Imaging Spectroradiometer (MODIS) and Multi-angle Imaging  
40 SpectroRadiometer (MISR) and surface AOD observations from AErosol RObotic NETwork  
41 (AERONET) shows reasonable agreements between simulated and observed AOD. However,  
42 BCC-ESM1 shows weaker upward transport of aerosols from the surface to the middle and  
43 upper troposphere, likely reflecting the deficiency of representing deep convective transport  
44 of chemical species in BCC-ESM1. With an overall good agreement between BCC-ESM1  
45 simulated and observed aerosol properties, it demonstrates a success of the implementation of  
46 interactive aerosol and atmospheric chemistry in BCC-ESM1.

47

## 48 **1. Introduction**

49        Atmosphere is a thin gaseous layer around the Earth, consisting of nitrogen, oxygen and  
50 a large number of trace gases including important greenhouse gases (GHG) such as water  
51 vapor, tropospheric ozone (O<sub>3</sub>), carbon dioxide (CO<sub>2</sub>), methane (CH<sub>4</sub>), nitrous oxide (N<sub>2</sub>O),  
52 and chloro-fluoro-carbons (CFCs). Besides gaseous components, atmosphere also contains  
53 various aerosols, which are important for cloud formation and radiative transfer. Atmospheric  
54 trace gases and aerosols are actually interactive components of the climate system. Their  
55 inclusion in global climate models (GCMs) is a significant enhancement for most  
56 state-of-the-art climate models (Lamarque et al., 2013; Collins et al., 2017). Early attempts in  
57 coupling global climate dynamics with atmospheric chemistry can be traced back to late  
58 1970s, when 3D transport of ozone and simple stratospheric chemistry were firstly  
59 incorporated into a GCM to simulate global O<sub>3</sub> production and transport (e.g., Cunnold et al.  
60 1975; Schlesinger and Mintz 1979). Since mid-1980s, a large number of on-line global  
61 climate/chemistry models have been developed to address issues of the Antarctic stratospheric  
62 O<sub>3</sub> depletion (e.g., Cariolle et al. 1990; Austin et al. 1992; Solomon, 1999), tropospheric O<sub>3</sub>  
63 and sulfur cycle (e.g., Feichter et al. 1996; Barth et al. 2000), tropospheric aerosol and its  
64 interactions with cloud (e.g., Chuang et al. 1997; Lohmann et al. 2000; Ghan and Easter, 2006;  
65 Jacobson 2012). Aerosols and chemically reactive gases in the atmosphere exert important  
66 influences on global and regional air quality and climate (Collins et al., 2017).

67        Since 2013, the Beijing Climate Center (BCC), China Meteorological Administration,  
68 has continuously developed and updated its fully-coupled GCM, the Beijing Climate Center  
69 Climate System Model (BCC-CSM) (Wu et al., 2013; Wu et al., 2014; Wu et al., 2019).  
70 BCC-CSM version 1.1 was one of the comprehensive carbon-climate models participating in  
71 the phase five of the Coupled Model Intercomparison Project (CMIP5, Taylor et al. 2012).  
72 When forced by prescribed historical emissions of CO<sub>2</sub> from combustion of fossil fuels and  
73 land use change, BCC-CSM1.1 successfully reproduced the trends of observed atmospheric  
74 CO<sub>2</sub> concentration and global surface air temperature from 1850 to 2005 (Wu et al., 2013).  
75 During recent years, BCC-CSM1.1 has been used in numerous investigations on soil organic  
76 carbon changes (e.g. Todd-Brown et al., 2014), ocean biogeochemistry changes (e.g. Mora et  
77 al., 2013), and carbon-climate feedbacks (e.g. Arora et al., 2013; Hoffman et al., 2014).

78 BCC-CSM includes main climate-carbon cycle processes (Wu et al., 2013) and the global  
79 mean atmospheric CO<sub>2</sub> concentration is calculated from a prognostic equation of CO<sub>2</sub> budget  
80 taking into account global anthropogenic CO<sub>2</sub> emissions and interactive land-atmosphere and  
81 ocean-atmosphere CO<sub>2</sub> exchanges.

82 In recent years, BCC has put large efforts in developing a global  
83 climate-chemistry-aerosol fully-coupled Earth System Model (BCC-ESM1) on the basis of  
84 BCC-CSM2 (Wu et al., 2019). The objective is to interactively simulate global aerosols (e.g.  
85 sulfate, black carbon, etc.) and main greenhouse gases (e.g. O<sub>3</sub>, CH<sub>4</sub>, NO<sub>2</sub> and CO<sub>2</sub>) in the  
86 atmosphere and to investigate feedbacks between climate and atmospheric chemistry.  
87 BCC-ESM1 is at the point to be publicly released, and it is actively used by BCC for several  
88 CMIP6-endorsed research initiatives (Eyring et al. 2016), including the Aerosol Chemistry  
89 Model Intercomparison Project (AerChemMIP, Collins et al., 2017) and the Coupled  
90 Climate–Carbon Cycle Model Intercomparison Project (C4MIP, Jones et al. 2016).

91 The purpose of this paper is to evaluate the performance of BCC-ESM1 in simulating  
92 aerosols and their optical properties in the 20th century. The description of BCC-ESM1 is  
93 presented in Section 2. The experimental protocol is given in Section 3. Section 4 presents the  
94 evaluations of aerosol simulations with comparisons to CMIP5-recommended data (Lamarque  
95 et al., 2010) and data obtained from both global surface networks and satellite observations.  
96 The regional and global characteristics compared to observations and estimates from other  
97 studies are analyzed. Simulations of aerosol optical properties in the 20th century are also  
98 analyzed in Section 4. Conclusions and discussions are summarized in Section 5. Information  
99 about code and data availability is given in Section 6.

## 100 **2. Model description**

101 BCC-ESM1 is an Earth System Model with interactive chemistry and aerosol  
102 components, in which the atmospheric component is BCC Atmospheric General Model  
103 version 3 (Wu et al., 2019) with interactive atmospheric chemistry (hereafter  
104 BCC-AGCM3-Chem), land component BCC Atmosphere and Vegetation Interaction Model  
105 version 2.0 (hereafter BCC-AVIM2.0), ocean component Modular Ocean Model version 4  
106 (MOM4)-L40, and sea ice component [sea ice simulator (SIS)]. Different components of  
107 BCC-ESM1 are fully coupled and interact with each other through fluxes of momentum,

108 energy, water, carbon and other tracers at their interfaces. The coupling between the  
109 atmosphere and the ocean is done every hour.

110 The atmospheric component BCC-AGCM3-Chem is able to simulate global atmospheric  
111 composition and aerosols from anthropogenic emissions as forcing agents. Its resolution is T42  
112 (approximately  $2.8125 \times 2.8125^\circ$  transformed spectral grid). The model has 26 levels in a hybrid  
113 sigma/pressure vertical coordinate system with the top level at 2.914 hPa. Details of the model  
114 physics are described in Wu et al. (2019). The BCC-AGCM3-Chem combines 66 gas-phase  
115 chemical species and 13 bulk aerosol compounds as listed in Table 1. Apart from 3 gas-phase  
116 species of dimethyl sulfide (DMS),  $\text{SO}_2$  and  $\text{NH}_3$ , the other 63 gas-phase species are the same  
117 as those in the “standard version” of MOZART2 (Model for Ozone and Related chemical  
118 Tracers, version 2), a global chemical transport model for the troposphere developed by the  
119 National Center for Atmospheric Research (NCAR) driven by meteorological fields from  
120 either climate models or assimilations of meteorological observations (Horowitz et al., 2003).  
121 Advection of all tracers in BCC-AGCM3-Chem is performed through a semi-Lagrangian  
122 scheme (Williamson and Rasch, 1989), and vertical diffusion within the boundary layer  
123 follows the parameterization of Holtslag and Boville (1993). The gas-phase chemistry of the  
124 63 MOZART2 gas-phase species as listed in Table 1 is treated in the same way as that in the  
125 “standard version” of MOZART2 (Horowitz et al., 2003), and there are 33 photolytic  
126 reactions and 135 chemical reactions involving 30 dry deposited chemical species and 25  
127 soluble gas-phase species. Dry deposition velocities for the 15 trace gases including  $\text{O}_3$ , CO,  
128  $\text{CH}_4$ ,  $\text{CH}_2\text{O}$ ,  $\text{CH}_3\text{OOH}$ ,  $\text{H}_2\text{O}_2$ ,  $\text{NO}_2$ ,  $\text{HNO}_3$ , PAN,  $\text{CH}_3\text{COCH}_3$ ,  $\text{CH}_3\text{COOOH}$ ,  $\text{CH}_3\text{CHO}$ ,  
129  $\text{CH}_3\text{COCHO}$ , NO, and  $\text{HNO}_4$  are not computed interactively and directly interpolated from  
130 MOZART2 climatological monthly mean deposition velocities  
131 ([https://en.wikipedia.org/wiki/MOZART\(model\)](https://en.wikipedia.org/wiki/MOZART(model))) which are calculated offline (Bey et al., 2001;  
132 Shindell et al., 2008) using a resistance-in-series scheme originally described in Wesely  
133 (1989). The dry deposition velocities for the other 15 species including MPAN, ONIT, ONITR,  
134  $\text{C}_2\text{H}_5\text{OH}$ , POOH,  $\text{C}_2\text{H}_5\text{OOH}$ ,  $\text{C}_3\text{H}_7\text{OOH}$ , ROOH, GLYALD, HYAC,  $\text{CH}_3\text{OH}$ , MACROOH,  
135 ISOPOOH, XOOH, HYDRALD, and  $\text{H}_2$  are calculated using prescribed deposition velocities  
136 of  $\text{O}_3$ , CO,  $\text{CH}_3\text{CHO}$ , or land surface type and surface temperature following the MOZART2  
137 (Horowitz et al., 2003). Wet removals by in-cloud scavenging for 25 soluble gas-phase species

138 in the “standard version” of MOZART2 use the parameterization of Giorgi and Chameides  
139 (1985) based on their temperature dependent effective Henry’s law constants. In-cloud  
140 scavenging is proportional to the amount of cloud condensate converted to precipitation, and  
141 the loss rate depends on the amount of cloud water, the rate of precipitation formation, and the  
142 rate of tracer uptake by the liquid phase water. Other highly soluble species such as HNO<sub>3</sub>,  
143 H<sub>2</sub>O<sub>2</sub>, ONIT, ISOPOOH, MACROOH, XOOH, and Pb-210 are also removed by below-cloud  
144 washout as calculated using the formulation of Brasseur et al. (1998). Below-cloud  
145 scavenging is proportional to the precipitation flux in each model layer and the loss rate  
146 depends on the precipitation rate. Vertical transport of gas tracers and aerosols due to deep  
147 convection is not yet included in the present version of BCC-AGCM3-Chem, which process  
148 is considered as a part of the deep convection and occurs generally in a small spatial region on  
149 a GCM-box with low-resolution (2.8 °lat. × 2.8 °lon.). Another consideration is that a large  
150 uncertainty exists to treat transport of those water-soluble tracers by deep convection. But this  
151 effect will be involved in the next version of BCC model.

152 The BCC-AVIM2.0 is the land model with terrestrial carbon cycle. It is described in  
153 details in Li et al. (2019) and includes biophysical, physiological, and soil carbon-nitrogen  
154 dynamical processes. The terrestrial carbon cycle operates through a series of biochemical  
155 and physiological processes on photosynthesis and respiration of vegetation. Biogenic  
156 emissions from vegetation are computed online in BCC-AVIM2.0 following the algorithm of  
157 the Model of Emissions of Gases and Aerosols from Nature version 2.1 (MEGAN2.1,  
158 Guenther et al., 2012).

159 The oceanic component of BCC-ESM1 is the Modular Ocean Model version 4 with 40  
160 levels (hereafter MOM4-L40), and the sea ice component Sea Ice Simulator (SIS).  
161 MOM4-L40 uses a tripolar grid of horizontal resolution with 1 °longitude by 1/3 °latitude  
162 between 30 °S and 30 °N ranged to 1 °longitude by 1 °latitude from 60 °S and 60 °N poleward  
163 and 40 z-levels in the vertical. Carbon exchange between the atmosphere and the ocean are  
164 calculated online in MOM4-L40 using a biogeochemistry module that is based on the  
165 protocols from the Ocean Carbon Cycle Model Intercomparison Project–Phase 2 (OCMIP2,  
166 <http://www.ipsl.jussieu.fr/OCMIP/phase2/>). SIS has the same horizontal resolution as  
167 MOM4-L40 and three layers in the vertical, including one layer of snow cover and two layers

168 of equally sized sea ice. Details of oceanic component MOM4-L40 and sea-ice component  
169 SIS that are used in BCC-ESM1 may be found in Wu et al. (2013) and Wu et al. (2019).

170 In the following sub-sections, we will describe the treatments in BCC-ESM1 for 3  
171 gas-phase species of DMS, SO<sub>2</sub> and NH<sub>3</sub>, 13 prognostic aerosol species including sulfate  
172 (SO<sub>4</sub><sup>2-</sup>), 2 types of organic carbon (hydrophobic OC1, hydrophilic OC2), 2 types of black  
173 carbon (hydrophobic BC1, hydrophilic BC2), 4 categories of soil dust (DST01, DST02,  
174 DST03, DST04), and 4 categories of sea salt (SSLT01, SSLT02, SSLT03, SSLT04).  
175 Concentrations of all aerosols in BCC-ESM1 are mainly determined by advective transport,  
176 emission, dry deposition, gravitational settling, and wet scavenging by clouds and  
177 precipitation, except for SO<sub>4</sub><sup>2-</sup> which gas-phase and aqueous phase conversion from SO<sub>2</sub> are  
178 also considered. The present version of aerosol scheme belongs to a bulk aerosol model and  
179 mainly refers to the scheme of CAM-Chem (Lamarque et al., 2012), but the nucleation and  
180 coagulation of aerosols are still ignored.

## 181 **2.1 SO<sub>2</sub>, DMS, NH<sub>3</sub>, and Sulfate**

182 SO<sub>2</sub> is a main sulfuric acid precursor to form aerosol sulfate SO<sub>4</sub><sup>2-</sup>. Conversions of SO<sub>2</sub>  
183 to SO<sub>4</sub><sup>2-</sup> occur by gas phase reactions (Table 2) and by aqueous phase reactions in cloud  
184 droplets. The dry deposition velocity of SO<sub>2</sub> follows the resistance-in-series approach of  
185 Wesely (1989) using the formula,  $W_{SO_2} = 1/(r_a + r_b + r_c)$ , in which  $r_a$ ,  $r_b$ , and  $r_c$  are the  
186 aerodynamic resistance, the quasi-laminar boundary layer resistance, and the surface  
187 resistance, respectively and they are interactively computed in each model time step. The loss  
188 rate of SO<sub>2</sub> due to wet deposition is computed following the scheme in the global Community  
189 Atmosphere Model (CAM) version 4, the atmospheric component of the Community Earth  
190 System Model (Lamarque et al., 2012).

191 The sources of SO<sub>2</sub> mainly come from fuel combustion, industrial activities, and  
192 volcanoes. SO<sub>2</sub> can also be formed from the oxidation of DMS as listed in Table 2 in which  
193 their reaction rates follow CAM-Chem (Lamarque et al. 2012). The main source of DMS is  
194 from oceanic emissions via biogenic processes. It is prescribed with the climatological  
195 monthly data that are extracted from MOZART2 package  
196 (<https://www2.acom.ucar.edu/gcm/mozart-4>). SO<sub>4</sub><sup>2-</sup> is one of the prognostic aerosols in  
197 BCC-AGCM3-Chem. Its treatment follows CAM4-Chem (Lamarque et al., 2012). It is

198 produced primarily by the gas-phase oxidation of SO<sub>2</sub> (in Table 2) and by aqueous phase  
199 oxidation of SO<sub>2</sub> in cloud droplets. The gas phase reactions, rate constants, and gas-aqueous  
200 equilibrium constants are given by Tie et al. (2001). The heterogeneous reactions of SO<sub>4</sub><sup>2-</sup>  
201 occur on all aerosol surfaces. Their treatment follows a Bulk Aerosol Model (BAM) used in  
202 CAM4 (Neale et al., 2010). The heterogeneous reactions depend strongly on pH values in  
203 clouds which are calculated from the concentrations of SO<sub>2</sub>, HNO<sub>3</sub>, H<sub>2</sub>O<sub>2</sub>, NH<sub>3</sub>, O<sub>3</sub>, HO<sub>2</sub>, and  
204 SO<sub>4</sub><sup>2-</sup>. NH<sub>3</sub> is a gas tracer apart from MOZART2 (Table 1). Its sources include aircraft and  
205 surface emissions due to anthropogenic activity, biomass burning, and biogenic emissions  
206 from land soil and ocean surfaces (Table 4). SO<sub>4</sub><sup>2-</sup> is assumed to be all in aqueous phase due  
207 to water uptake, although Wang et al. (2008a) showed that ~34% of sulfate particles are in  
208 solid phase globally due to the hysteresis effect of ammonium sulfate phase transition.  
209 However, in terms of radiative forcing, consideration of solid sulfate formation process  
210 lowers the sulfate forcing by ~8% as compared to consideration of all sulfate particles in  
211 aqueous phase (Wang et al., 2008b). Future model development may consider the life cycle of  
212 NH<sub>3</sub>. The sulfate in- and below-cloud scavenging follows Neu and Prather (2011). Washout  
213 of SO<sub>4</sub><sup>2-</sup> is set to 20% of the washout rate of HNO<sub>3</sub> following Tie et al. (2005) and Horowitz  
214 (2006). Dry deposition velocity of SO<sub>4</sub><sup>2-</sup> is also calculated by the resistance-in-series  
215 approach.

## 216 **2.2 Aerosols of organic carbon and black carbon**

217 BCC-AGCM3-Chem treats two types of organic carbon (OC), i.e. water-insoluble tracer  
218 OC1 and water-soluble tracer OC2, and two types of black carbon (BC), i.e. water-insoluble  
219 tracer BC1 and water-soluble tracer BC2. As shown in Table 2, hydrophobic BC1 and OC1  
220 can be converted to hydrophilic BC2 and OC2 with a constant rate of  $7.1 \times 10^{-6} \text{ s}^{-1}$  (Cooke and  
221 Wilson, 1996). The 4 tracers of organic carbon and black carbon are mainly from emissions  
222 including both fossil fuel and biomass burning, and are from the CMIP6 data package  
223 (<https://esgf-node.llnl.gov/search/input4mips/>, Hoesly et al., 2018). Beside anthropogenic and  
224 biomass burning emissions, hydrophilic organic carbon OC2 can also come from natural  
225 biogenic volatile organic compound (VOC) emissions. Dry deposition velocities for all the 4  
226 OC and BC tracers are set to  $0.001 \text{ m.s}^{-1}$ . OC2 and BC2 are soluble aerosols, and their sinks  
227 are primarily governed by wet deposition. Their in- and below-cloud scavenging follows the



228 scheme of Neu and Prather (2011).

### 229 **2.3 Sea salt aerosols**

230 As shown in Table 3, sea salt aerosols in the model are classified into four size bins (0.2–  
231 1.0, 1.0–3.0, 3.0–10, and 10–20  $\mu\text{m}$ ) in diameter. They originate from oceans and are  
232 calculated online by BCC-ESM1. The upward flux  $F_{sea-salt}$  of sea salt productions for four  
233 bins is proportional to the 3.41 power of the wind speed  $u_{10m}$  at 10 m height near the sea  
234 surface (Mahowald et al., 2006) and is expressed as

$$235 \quad F_{sea-salt} = S \cdot (u_{10m})^{3.41}, \quad (1)$$

236 where  $S$  is a scaling factor and set to  $4.05 \times 10^{-15}$ ,  $4.52 \times 10^{-14}$ ,  $1.15 \times 10^{-13}$ ,  $1.20 \times 10^{-13}$  for four  
237 size bins of sea salt aerosols in BCC-ESM1, respectively.

238 Dry deposition of sea salts depends on the turbulent deposition velocity in the lowest  
239 atmospheric layer using aerodynamic resistance and the friction velocity, and the settling  
240 velocity through the whole atmospheric column for each bin of sea salts. The turbulent  
241 deposition velocity and settling velocity depend on particle diameter and density (listed in  
242 Table 3). In addition, the fact that the size of sea salts changes with humidity is also  
243 considered. The wet deposition of sea salts follows the scheme for soluble aerosols used in  
244 CAM4, and depends on prescribed solubility and size-independent scavenging coefficients.

### 245 **2.4 Dust aerosols**

246 Dust aerosols behave in a similar way as sea salts. Their variations involve three major  
247 processes: emission, advective transport, and wet/dry depositions. The dust emission is based  
248 on a saltation-sandblasting process, and depends on wind friction velocity, soil moisture, and  
249 vegetation/snow cover (Zender et al., 2003). The vertical flux of dust emission is corrected by  
250 a surface erodible factor at each model grid cell which has been downloaded from NCAR  
251 website (<https://svn-ccsm-inputdata.cgd.ucar.edu/trunk/inputdata/atm/cam/dst/>). Soil  
252 erodibility is prescribed by a physically-based geomorphic index that is proportional to the  
253 runoff area upstream of each source region (Albani et al., 2014). Like sea salts, dry deposition  
254 of dust aerosols includes gravitational and turbulent deposition processes, while wet  
255 deposition results from both convective and large scale precipitation and is dependent on  
256 prescribed size-independent scavenging coefficients.

### 257 **2.5 Effects of aerosols on radiation, clouds, and precipitation**

258 The mass mixing ratios of bulk aerosols are prognostic variables in BCC-ESM1 and  
 259 directly affect the radiative transfer in the atmosphere with their treatments following the  
 260 NCAR Community Atmosphere Model (CAM3, Collins et al., 2004). Indirect effects of  
 261 aerosols are taken into account in the present version of BCC-AGCM3-Chem (Wu et al.,  
 262 2019). Aerosol particles act as cloud condensation nuclei and exert influence on cloud  
 263 properties and precipitation, and ultimately impact the hydrological cycle.

264 Prognostic aerosol masses are used to estimate the liquid cloud droplet number  
 265 concentration  $N_{cdnc}$  ( $\text{cm}^{-3}$ ) in BCC-AGCM3-Chem.  $N_{cdnc}$  is explicitly calculated using the  
 266 empirical function suggested by Boucher and Lohmann (1995) and Quaas et al. (2006):

$$267 \quad N_{cdnc} = \exp[5.1 + 0.41 \ln(m_{aero})] \quad (2)$$

268 where  $m_{aero}$  ( $\mu\text{g}\cdot\text{m}^{-3}$ ) is the total mass of all hydrophilic aerosols,

$$269 \quad m_{aero} = m_{SS} + m_{OC} + m_{SO_4} + m_{NH_4NO_2}, \quad (3)$$

270 i.e. the first bin of sea salt ( $m_{SS}$ ), hydrophilic organic carbon ( $m_{OC}$ ), sulphate ( $m_{SO_4}$ ), and  
 271  $NH_4NO_2$ . A dataset of  $NH_4NO_2$  from NCAR CAM-Chem (Lamarque et al., 2012) is used in  
 272 our model.

273  $N_{cdnc}$  is an important factor in determining the effective radius of cloud droplets for  
 274 radiative calculation. The effective radius of cloud droplets  $r_{el}$  is estimated as

$$275 \quad r_{el} = \beta \cdot r_{l,vol}, \quad (4)$$

276 where  $\beta$  is a parameter dependent on the droplets spectral shape and follows the calculation  
 277 proposed by Peng and Lohmann (2003),

$$278 \quad \beta = 0.00084 N_{cdnc} + 1.22. \quad (5)$$

279  $r_{l,vol}$  is the volume-weighted mean cloud droplet radius,

$$280 \quad r_{l,vol} = \left[ \frac{(3LWC)}{(4\pi\rho_w N_{cdnc})} \right]^{1/3}, \quad (6)$$

281 where  $\rho_w$  is the liquid water density and  $LWC$  the cloud liquid water content ( $\text{g cm}^{-3}$ ).

282 Aerosols also exert impacts on precipitation efficiency (Albrecht, 1989), which is taken  
 283 into account in the parameterization of non-convective cloud processes. There are five  
 284 processes that convert condensate to precipitate: auto-conversion of liquid water to rain,  
 285 collection of cloud water by rain, auto-conversion of ice to snow, collection of ice by snow,

286 and collection of liquid by snow. The auto-conversion of cloud liquid water to rain (*PWAUT*)  
 287 is dependent on the cloud droplet number concentration and follows a formula that was  
 288 originally suggested by Chen and Cotton (1987),

$$289 \quad PWAUT = C_{l,aut} \hat{q}_l^2 \rho_a / \rho_w \left( \frac{\hat{q}_l \rho_a}{\rho_w N_{ncdc}} \right)^{1/3} H(r_{l,vol} - r_{lc,vol}) \quad (7)$$

290 Where  $\hat{q}_l$  is in-cloud liquid water mixing ratio,  $\rho_a$  and  $\rho_w$  are the local densities of air and  
 291 water respectively, and  $C_{l,aut}$  is a constant.  $H(x)$  is the Heaviside step function with the  
 292 definition,

$$293 \quad H(x) = \begin{cases} 0, & x < 0 \\ 1, & x \geq 0 \end{cases}. \quad (8)$$

294  $r_{lc,vol}$  is the critical value of mean volume radius of liquid cloud droplets  $r_{l,vol}$ , and set to 15  
 295  $\mu$  m.

296

### 297 **3. Experiment design for the 20<sup>th</sup> century climate simulation**

298 There is an Aerosol Chemistry Model Intercomparison Project (AerChemMIP, Collins et  
 299 al., 2017) endorsed by the Coupled-Model Intercomparison Project 6 (CMIP6) for  
 300 documenting and understanding past and future changes in the chemical composition of the  
 301 atmosphere, and estimating the global-to-regional climate response from these changes.  
 302 Modelling groups with full chemistry and aerosol models are encouraged to perform all  
 303 AerChemMIP simulations (Collins et al., 2017). To assess the ability of our model to simulate  
 304 aerosols (mean and variability), we have followed the historical simulation designed by  
 305 CMIP6 (Eyring et al., 2016) which is named as “historical” experiment in the Earth System  
 306 Grid Federation (ESGF). The protocol details of the historical experiment forced with  
 307 emissions evolving from 1850 to 2014 refer to Collins et al. (2017).  $O_3$  in the historical  
 308 simulation is an interactive prognostic variable and feedbacks on radiation, and the  
 309 concentrations of other WMOGHG, e.g.  $CH_4$ ,  $N_2O$ ,  $CO_2$ , CFC11, and CFC12 are prescribed  
 310 using CMIP6 historical forcing data as suggestion in AerChemMIP protocol. Although  $CH_4$   
 311 and  $N_2O$  are prognostic variables in the chemistry scheme (Table 1), their prognostic values at  
 312 each model step in the historical experiment are replaced by CMIP6 data. The rest of  
 313 historical forcing data include: (1) yearly global gridded land-use forcing data sets, and (2)

314 solar forcing. All these datasets were downloaded from  
315 <https://esgf-node.llnl.gov/search/input4mips/>. Climate feedback processes that involve changes  
316 to the atmospheric composition of reactive gases and aerosols may affect the temperature  
317 response to a given WMGHG concentration level (Collins et al., 2017). Three members of  
318 historical experiments are conducted and the first member is analyzed in this work.

### 319 **3.1 Surface emissions**

320 Surface emissions of chemical species from different sources are summarized in Table  
321 4. They include anthropogenic emissions from fossil fuel burning and other industrial  
322 activities, biomass burning (including vegetation fires, fuel wood and agricultural burning),  
323 biogenic emissions from vegetation and soils, and oceanic emissions. Most historical  
324 emissions from anthropogenic source (surface, aircraft plus ship) and biomass burning from  
325 1850 to 2014 are CMIP6-recommended data (Hoesly et al., 2018; available at  
326 <https://esgf-node.llnl.gov/search/input4mips/>). Anthropogenic or biomass burning sources of  
327 some tracers which are not included in the CMIP6 dataset (see Table 4), anthropogenic  
328 emission of H<sub>2</sub> and N<sub>2</sub>O are from monthly climatological dataset provided by the MOZART-2  
329 standard package. N<sub>2</sub>O is a prognostic variable in BCC-ESM1 but it is replaced by CMIP6  
330 prescribed concentration in the historical run. Other emissions including biomass burning  
331 (CH<sub>3</sub>COCH<sub>3</sub>) and anthropogenic emission (CH<sub>3</sub>CHO, CH<sub>3</sub>OH, and CH<sub>3</sub>COCH<sub>3</sub>) are from the  
332 IPCC ACCMIP emission inventory (<http://accent.aero.jussieu.fr/ACCMIP.php>) covering the  
333 period from 1850 to 2010 with 10-year intervals (see Table 4). Monthly lumped emissions of  
334 black carbon and organic carbon aerosols from 1850 to 2014 are downloaded from  
335 CMIP6-recommended data, but we used 80% (for BC) and 50% (for OC) of them in their  
336 hydrophobic forms (BC1 and OC1) and the rest in their hydrophilic forms (BC2 and OC2),  
337 following the work of Chin et al. (2002).

338 Five tracers of ISOP, ACET (CH<sub>3</sub>COCH<sub>3</sub>), C<sub>2</sub>H<sub>4</sub>, C<sub>3</sub>H<sub>8</sub>, and Monoterpenes (C<sub>10</sub>H<sub>16</sub>) in  
339 Table 1 belong to biogenic volatile organic carbons (VOCs). As shown in Table 4, those  
340 VOCs emissions are online calculated in BCC-ESM1 following the modeling framework of  
341 the Model of Emissions of Gases and Aerosols from Nature version 2.1 (MEGAN2.1,  
342 Guenther et al., 2012) using simple mechanistic algorithms to account for major known  
343 processes controlling biogenic emissions. The MEGAN2.1 can provide a flexible scheme for

344 estimating 16 tracers of biogenic emissions from terrestrial ecosystems including five VOCs  
345 emissions used in BCC-ESM1 (Table 4). All the VOCs emissions depend on current and past  
346 surface air temperature, solar flux, and the landscape types. Their calculation requires global  
347 maps of plant functional type (PFT) and leaf area index (LAI) which is a prognostic variable  
348 from the land model BCC-AVIM2. The effect of atmospheric CO<sub>2</sub> concentration on isoprene  
349 emissions is included. 10% of the biogenic monoterpenes emissions as calculated online with  
350 the MEGAN2.1 algorithm in BCC-AVIM2 are converted to hydrophilic organic carbon (OC<sub>2</sub>)  
351 to account for formation of secondary organic aerosols following Chin et al. (2002) in this  
352 version of BCC-ESM1.

### 353 **3.2 Volcanic eruption, lightning and aircraft emissions**

354 As there is no stratospheric aerosol scheme in BCC-ESM1, concentrations of sulfate  
355 aerosol at heights from 5 to 39.5 km, which volcanic origin, are directly prescribed using the  
356 CMIP6-recommended data (Thomasson et al., 2018) from 1850 to 2014. The effects of  
357 surface SO<sub>2</sub> emissions from volcanic eruption on the variation of SO<sub>2</sub> in the atmosphere and  
358 then on the variation of tropospheric SO<sub>4</sub><sup>2-</sup> concentration are considered, and the SO<sub>2</sub>  
359 emissions from 1850 to 2014 are downloaded from the IPCC ACCMIP emission inventory  
360 (<http://accent.aero.jussieu.fr/ACCMIP.php>). Aircraft emissions are provided for NO<sub>2</sub>, CO,  
361 CH<sub>4</sub>, NH<sub>3</sub>, NO, SO<sub>2</sub>, and aerosols of OC and BC (Table 1). The emissions of NO from  
362 lightning are online calculated in BCC-AGCM3-Chem following the parameterization in  
363 MOZART2, and the globally-averaged mean during the period of 1850 to 2014 is 5.19  
364 Tg(N) yr<sup>-1</sup>, which is in agreement with observations within the range of 3 to 6 Tg(N) yr<sup>-1</sup>  
365 (Martin et al., 2002). The lightning frequency depends strongly on the convective cloud top  
366 height, and the ratio of cloud-to-cloud versus cloud-to-ground lightning depends on the cold  
367 cloud thickness from the level of 0°C to the cloud top (Price and Rind, 1992).

### 368 **3.3 Upper boundary of the atmosphere**

369 As no stratospheric chemistry is included in the present version of BCC-AGCM3-Chem,  
370 it is necessary to ensure a proper distribution of chemically-active stratospheric species.  
371 Concentrations of different tracers (O<sub>3</sub>, CH<sub>4</sub>, N<sub>2</sub>O, NO, NO<sub>2</sub>, HNO<sub>3</sub>, CO, and N<sub>2</sub>O<sub>5</sub>) at the top  
372 two layers of the model are set to prescribed monthly climatological values, and  
373 concentrations from below the top two layers to the tropopause are relaxed at a relaxation

374 time of 10-days towards the climatology. Climatological values of NO, NO<sub>2</sub>, HNO<sub>3</sub>, CO and  
375 N<sub>2</sub>O<sub>5</sub> at the top two layers are extracted from MOZART2 data package available at the  
376 Website (<https://www2.acom.ucar.edu/gcm/mozart-4>), originated from the Study of Transport  
377 and Chemical Reactions in the Stratosphere (STARS, Brasseur et al., 1997). Concentrations  
378 for the other tracers (O<sub>3</sub>, CH<sub>4</sub>, and N<sub>2</sub>O) at the top two model layers are the zonally-averaged  
379 and monthly values from 1850 to 2014 derived from the CMIP6 data package.

### 380 **3.4 The preindustrial model states**

381 The preindustrial state of BCC-ESM1 is obtained from a piControl simulation of over 600  
382 years in which all forcings including emissions data are fixed at 1850 conditions. The initial  
383 state of the piControl simulation itself is obtained through individual spin-up runs of each  
384 component of BCC-ESM1 in order for the piControl simulation to run stably and fast to reach  
385 its equilibrium. Figures 1(a-c) show the time series of global yearly means of the net energy  
386 budget at top of the atmosphere (TOA), near-surface air temperature (TAS), and sea surface  
387 temperature (SST) from the piControl simulation for the last 450 years. It shows that the  
388 surface climate in BCC-ESM1 nearly reaches its equilibrium after 600 years piControl  
389 simulation. The whole system in BCC-ESM1 fluctuates around +0.7 Wm<sup>-2</sup> net energy flux at  
390 TOA without obvious trend in 450 years (Fig. 1a). This level of TOA energy imbalance is  
391 close to the average imbalance (1.0 Wm<sup>-2</sup>) among CMIP5 models (Wild et al., 2013), and do  
392 not cause remarkable climate drift in BCC-ESM1. The global mean TAS and SST keep  
393 around 288.1 K (Fig. 1b) and 295.05 K (Fig. 1c), respectively. During the last 450 years, there  
394 are ( $\pm 0.2$  K amplitude of TAS and SST) oscillations of centennial scale for the whole globe  
395 (Figs. 1b and 1c), which are certainly caused by internal variation of the system.

396 Figures 2a-2c show the time series of global annual total burdens of SO<sub>2</sub>, DMS, and OH  
397 in the troposphere (integrated from the surface to 100 hPa) in the last 450 years of the  
398 piControl simulation. Without any anthropogenic source, the SO<sub>2</sub> amount in the troposphere  
399 nearly keeps the level of 0.0868 Tg in the 450 years of the piControl simulation. Tropospheric  
400 DMS varies around the value of 0.116 Tg. Tropospheric OH, as an important gas species  
401 oxidizing SO<sub>2</sub> to form SO<sub>4</sub><sup>2-</sup> (Table 2), keeps at a stable level in the atmosphere. SO<sub>4</sub><sup>2-</sup> also  
402 remains at a stable level of 0.556 Tg in the atmosphere in the whole period of the piControl  
403 simulation (Figure 2d). The amounts of BC and OC in the troposphere vary around 0.0395 Tg

404 and 0.275 Tg (Figures 2e-2f), respectively. Dust and sea salt aerosols are at the level of 22 Tg  
405 and 11.7 Tg (Figures 2g-2h), respectively. All those data are close to the global mean  
406 concentrations of 0.604 Tg  $\text{SO}_4^{2-}$ , 0.046 Tg BC, 0.30 Tg OC, 22.18 Tg dust, and 11.73 Tg sea  
407 salts in 1850 which are estimated based on the CMIP5 prescribed data in 1850 (Lamarque et  
408 al., 2010).

409 Figure 3 shows the global spatial distributions of annual mean sulfate, organic carbon,  
410 black carbon, dust, and sea salt aerosols in the whole atmospheric column averaged for the  
411 last 100 years of the piControl simulation of BCC-ESM. We can compare them with CMIP5  
412 recommended concentrations in year 1850, considered as the reference state in the  
413 pre-industrial stage. At that time, there are fewer anthropogenic/biomass  $\text{SO}_2$  emissions, the  
414  $\text{SO}_4^{2-}$  over land are evidently smaller than those over oceans especially over the tropical  
415 Pacific and Atlantic Oceans, where DMS can be oxidized to  $\text{SO}_2$  and then form  $\text{SO}_4^{2-}$ . There  
416 are several centers of high values of black carbon and organic carbon in East and South Asia,  
417 Europe, Southeast America, and in the tropical rain forests in Africa and South America.  
418 They mainly result from biomass burning including vegetation fires, fuel wood and  
419 agricultural burning. Dust aerosols are mainly distributed in North Africa, Central Asia, North  
420 China, and Australia, where arid and semi-arid areas locate. Dust emitted from Sahara Desert  
421 can be transported to the tropical Atlantic by easterly wind. The sea salt aerosols are mainly  
422 distributed over the mid-latitude Southern Oceans, the tropical southern Indian Ocean, and the  
423 tropical northern Pacific Ocean, where wind speeds near the sea surface are strong. As shown  
424 in Fig. 3, all the spatial distribution patterns of CMIP5-derived sulfate, black carbon, organic  
425 carbon, dust, and sea salt aerosols (Lamarque et al., 2010) are well simulated in BCC-ESM1.  
426 There are high spatial correlation coefficients, 0.76 for sulfate, 0.77 for black carbon, 0.77 for  
427 organic carbon, 0.94 for dust, and 0.94 for sea salts, between CMIP5 data and BCC-ESM1  
428 simulations. Relative lower relations for sulfate, black carbon and organic carbon are possibly  
429 caused as different anthropogenic emission sources are used in BCC-ESM1 and to create  
430 CMIP5 data. Dust and sea salts belong to natural aerosols and depend on the land and sea  
431 surface conditions, so their spatial distributions are easy to be captured and have relatively  
432 higher correlations between CMIP5 data and BCC-ESM1 simulations.

433

#### 434 **4. Evaluation of O<sub>3</sub> and aerosol simulations in the 20<sup>th</sup> century**

435 The rate of sulfate formation is dependent on the levels of oxidants in the troposphere.  
436 O<sub>3</sub> is an important oxidant. So, the evaluation of simulated tropospheric O<sub>3</sub> is helpful to  
437 understand the aerosols simulations. BCC-ESM1 is driven by most of the  
438 CMIP6-recommended emission data. As shown in Figure 4, the zonal distributions of the total  
439 amounts of tropospheric O<sub>3</sub> below 300 hPa to the ground and their changes with time from  
440 1850 to 2014 from the CMIP6-recommend dataset (Table 4) are well simulated by  
441 BCC-ESM1. Evident increasing trends since 1850 almost exist in every latitudes, especially  
442 in the Northern Hemisphere where the contents of tropospheric O<sub>3</sub> are higher than those in the  
443 Southern Hemisphere.

444 Figure 5 shows the vertical profiles of O<sub>3</sub> simulations with comparison to global  
445 ozonesonde observations averaged for the monthly data over 2010-2014 from the World  
446 Ozone and Ultraviolet Radiation Data Centre (WOUDC; <http://woudc.org/data.php>, last  
447 access: 24 September 2019) in nine regions which are averaged from 41 global WOUDC sites.  
448 The details of WOUDC data may refer to Lu et al. (2019). As shown in Figure 5, BCC-ESM1  
449 well captures the observed ozone vertical structure at all regions. At the lower and middle  
450 troposphere (i.e. below 6 km), the model typically shows positive bias within 5 ppbv for the  
451 Southern Hemisphere and 10 ppbv for the Northern mid-latitudes, similar to those simulated  
452 from many other global atmospheric chemical models (Young et al., 2013, 2018). The model  
453 has larger ozone overestimation in the upper troposphere and stratosphere at most regions, at  
454 least partly due to the use of prescribed stratospheric ozone as upper boundary conditions  
455 and/or errors in modeling ozone exchange between the stratosphere and the troposphere.  
456 Global tropospheric ozone burden derived from our simulation is 335 Tg averaged over  
457 2010-2014, in consistent with recent assessment from multi chemistry models (Young et al.,  
458 2018).

#### 459 **4.1 Global aerosols trends**

460 Figure 6(a)-(c) show the time series of global total emissions of SO<sub>2</sub>, OC, and BC to the  
461 atmosphere from natural and anthropogenic sources. Emissions of SO<sub>2</sub> are largely due to  
462 industrial production. From 1850 to 1915, SO<sub>2</sub> emissions increased year by year as the  
463 Industrial Revolution intensified and expanded. But from 1915 to 1945, the increase trend of



464 SO<sub>2</sub> emissions became slower as broke out the First and the Second World Wars. After that  
465 period, with growing industrial productions, SO<sub>2</sub> emissions increased again and reached a  
466 maximum around the end of 1970s. During the 1980s and 2000s, with a substantial decrease  
467 of SO<sub>2</sub> emissions in Europe and the United States, the global SO<sub>2</sub> emissions has been  
468 decreasing since the 1980s despite the rapid increase of SO<sub>2</sub> emissions in South and East Asia  
469 as well as in developing countries in the Southern Hemisphere in recent years (Liu et al.,  
470 2009). The OC and BC emissions substantially increased since 1950s just after the Second  
471 World War. The global total OC emission in 2010 was nearly twice as much as that in  
472 pre-industrial (year 1850) and increased by 18 Tg • yr<sup>-1</sup>. Anthropogenic black carbon  
473 emissions increased from 1 Tg yr<sup>-1</sup> in 1850 to nearly 8 Tg yr<sup>-1</sup> in 2010.

474 Anthropogenic SO<sub>2</sub>, OC and BC emissions strongly affect the variations of atmospheric  
475 concentrations of sulfate, OC, and BC. The global 0.5°x0.5° gridded data of  
476 CMIP5-recommended aerosols masses with 10-years interval from 1850 to 2000 (Lamarque  
477 et al., 2010) provides an important reference to evaluate the aerosol simulations in  
478 BCC-ESM1. As shown in Figure 7b-7f, the annual total aerosol burdens of SO<sub>4</sub><sup>2-</sup>, OC, and BC  
479 in the whole atmosphere column as simulated by the BCC-ESM1 20<sup>th</sup> century historical  
480 simulation are generally consistent with the values derived from CMIP5-recommended  
481 aerosols concentrations. Due to increasing SO<sub>2</sub> emissions from 1850 to present day (Fig. 6),  
482 the global SO<sub>2</sub> burden in the atmosphere increased from 100 Tg in 1850s to 200 Tg in 1980s  
483 (Fig. 7a), and has a high correlation coefficient of 0.996 with the anthropogenic emissions  
484 (Fig. 6a), as the lifetime of SO<sub>2</sub> is short. The burden directly followed the emission. DMS in  
485 the atmosphere is oxidized by OH and NO<sub>3</sub> to form SO<sub>2</sub> (Table 2). Its natural emissions from  
486 oceans from 1850 to 2010 in the model are the climatological monthly means (Dentener et al.,  
487 2006) from MOZART2 data package. As shown in Fig 7a, the global amount of DMS in the  
488 whole atmosphere was about 0.12 Tg during 1850-1900 and decreased to 0.055 Tg in 2010.  
489 This decrease trend maybe partly results from the speeded rate of DMS oxidation with global  
490 warming, and the loss of DMS gradually exceeds the source of ocean DMS emission to cause  
491 a net loss of DMS in the atmosphere since 1910s. Largely driven by SO<sub>2</sub> anthropogenic  
492 emissions, the sulfate burden shows three different stages from 1850 to present. In the first  
493 period from 1850s to 1900s, the sulfate burden had a weak linear increase. It increased

494 significantly in the second stage from 1910's to 1940's, and then exploded since 1950's, until  
495 the middle 1970s and early 1980s. The sulfate burden then remained nearly stable and even  
496 showed slightly decreases as seen from the CMIP5 data. As for global BC and OC burdens,  
497 BCC-ESM1 results show continuous increases since 1850s, especially from 1950 to present.  
498 From 1910's to 1940's, the CMIP5 data show a slight decrease of BC and OC burdens in the  
499 atmosphere.

500 The dust and sea salt aerosols in the atmosphere are largely determined by the  
501 atmospheric circulations and states of the land and ocean surface. We can see that the global  
502 dust burden in the atmosphere showed evident increase from 1980 to 2000, which could be  
503 partly caused by evident global warming since 1980 and increasing soil dryness resulting in  
504 more surface dust to be released in the atmosphere. Their details will be explored in the other  
505 paper.

## 506 **4.2 Global aerosols budgets**

507 We further evaluate global aerosols budgets by comparing a 10-year average of  
508 BCC-ESM results from 1990 to 2000 with various studies for sulfate, BC, OC, sea salt, and  
509 dust. Their annual total emissions, average atmospheric mass loading, and mean lifetimes are  
510 listed in Tables 5 and 6. It is worth emphasizing that the global mean total source and sink for  
511 each type of aerosols in BCC-ESM1 are almost balanced.

512 The global DMS emission from the ocean is  $27.4 \text{ Tg(S) yr}^{-1}$  in BCC-ESM. This  
513 emission in BCC-ESM is nearly balanced by the gas-phase oxidation of DMS to form  $\text{SO}_2$ .  
514 The DMS burden is  $0.12 \text{ Tg}$  with a lifetime of 0.78 days, which is within the range of other  
515 models reported in the literature. As shown in Table 5, the total  $\text{SO}_2$  production averaged for  
516 the period of 1991 to 2000 is  $76.93 \text{ Tg(S) yr}^{-1}$ . A rate of  $13.2 \text{ Tg(S) yr}^{-1}$  (about 17%)  $\text{SO}_2$  is  
517 produced from the DMS oxidation, only  $0.1 \text{ Tg(S) yr}^{-1}$   $\text{SO}_2$  from airplane emissions to the  
518 atmosphere, and the rest ( $63.63 \text{ Tg(S) yr}^{-1}$ , near 82.7%) from anthropogenic activities and  
519 volcanic eruption at surface. The amount of  $\text{SO}_2$  produced from the DMS oxidation is in the  
520 range of other works ( $10.0$  to  $24.7 \text{ Tg(S) yr}^{-1}$ ) reported in Liu et al (2005). All the  $\text{SO}_2$   
521 production is balanced by  $\text{SO}_2$  losses by dry and wet deposition, and by gas- and  
522 aqueous-phase oxidation. Half of its loss ( $38.74 \text{ Tg(S) yr}^{-1}$ ) occurs via its aqueous-phase  
523 oxidation to form sulfate. Other losses through dry and wet depositions and gas-phase

524 oxidation to form  $\text{SO}_4^{2-}$  are also important (Table 2). All the sinks are in the range from the  
525 literature (Liu et al., 2005). The global burden of  $\text{SO}_2$  in the atmosphere is 0.48 Tg with a  
526 lifetime of 1.12 days, consistent with values in literature (Liu et al., 2005).

527 Sulfate aerosol is mainly produced from aqueous-phase  $\text{SO}_2$  oxidation ( $38.73 \text{ Tg(S) yr}^{-1}$ )  
528 and partly from gaseous phase oxidation of  $\text{SO}_2$  ( $10.32 \text{ Tg(S) yr}^{-1}$ ), and is largely lost by wet  
529 scavenging ( $49.06 \text{ Tg(S) yr}^{-1}$ ). The total  $\text{SO}_4^{2-}$  production in BCC-ESM is at the lower range  
530 of values in other models reported in Textor et al. (2006). Its global burden is 1.89 Tg and the  
531 lifetime is 4.69 days, which are within the range of 1.71 to 2.43 Tg and 3.3 to 5.4 days in the  
532 literatures (Textor et al., 2006; Liu et al., 2012; Liu et al., 2016; Matsui and Mahowald, 2017;  
533 Tegen et al., 2019; the value derived from CMIP5 data).

534 Sources of BC and OC are mainly from anthropogenic emissions. Based on the CMIP6  
535 data, there are, on average,  $7.22 \text{ Tg yr}^{-1}$  BC and  $13.91 \text{ Tg yr}^{-1}$  OC from fossil and bio-fuel  
536 emissions and  $18.38 \text{ Tg yr}^{-1}$  OC from natural emission during the period of 1991 to 2000.  
537 Most of them are scavenged through convective and large-scale rainfall processes. The rest  
538 returns to the surface by dry deposition. The simulated global BC and OC burdens are 0.13  
539 and 0.62 Tg, respectively (Table 6), all close to values of 0.114 Tg BC and 0.69 Tg OC  
540 derived from the CMIP5 data, and within the range of 0.11-0.26 Tg BC (Textor et al., 2006;  
541 Matsui and Mahowald, 2017; Tegen et al., 2019) and less than the values of 1.25-2.2 Tg OC  
542 in other literatures (Textor et al., 2006; Tegen et al., 2019). The simulated BC and OC  
543 lifetimes are 6.6 and 5.0 days respectively, and are close to the recent values of 5.0-7.5 days  
544 BC and 5.4-6.6 days OC in literatures (Matsui and Mahowald, 2017; Tegen et al., 2019).

545 The emissions of dust and sea salt are mainly determined by winds near the surface. The  
546 annual total dust emission in BCC-ESM1 is  $2592 \text{ Tg yr}^{-1}$ , higher than AeroCom multi-model  
547 mean ( $1840 \text{ Tg yr}^{-1}$ , Textor et al., 2006), but comparable to other studies (Chin et al., 2002;  
548 Liu et al., 2012; Matsui and Mahowald, 2017). The average dust loading is 22.93 Tg, lower  
549 than the value of 35.9 Tg in Ginoux et al. (2001) but slightly higher than the value of 20.41  
550 Tg derived from CMIP5 data. The average lifetime for dust particles is 3.23 days that is  
551 shorter than the AeroCom mean (4.14 days) and the value of 3.9 days in recent study (Matsui  
552 and Mahowald, 2017). The simulated sea salt emission is  $4667.2 \text{ Tg yr}^{-1}$ , slightly lower than  
553 the simulated value in Liu et al. (2012), and substantially lower than the AeroCom mean

554 (16600 Tg yr<sup>-1</sup>, Textor et al., 2006). The simulated sea salt burdens are 11.89 Tg and close to  
555 the CMIP5 data. Their averaged lifetimes are 0.93 days and close to the value in the recent of  
556 Matsui and Mahowald (2017) but longer than the AeroCom mean (0.41days, Textor et al.,  
557 2006).

### 558 **4.3 Global aerosol distributions at present day**

559 Figures 8-12 show December-January-February (DJF) and June-July-August (JJA) mean  
560 column mass concentrations of sulfate (SO<sub>4</sub><sup>2-</sup>), OC, BC, Dust, and Sea Salt aerosols averaged  
561 for the period of 1991-2000, respectively. Here, BCC-ESM1 simulated results are compared  
562 with the CMIP5-recommended data for the same period. Unlike the pre-industrial level of  
563 sulfate shown in Fig. 2, sulfate concentrations at present day (Fig. 8) are strongly influenced  
564 by anthropogenic emissions, and have maximum concentrations in the industrial regions (e.g.,  
565 East Asia, Europe, and North America). Their seasonal variations are distinct and are  
566 characterized by high concentrations in boreal summer and low concentrations in boreal  
567 winter. These spatial distributions simulated by BCC-ESM1 are well consistent with the  
568 CMIP5 data, with spatial correlation coefficients in DJF and JJA reaching 0.92 and 0.83  
569 (Figure 13), respectively. The deviation of the spatial pattern in BCC-ESM1 is less from the  
570 CMIP5 data in DJF but larger in JJA (Figure 13).

571 Unlike sulfate whose maximum concentrations are mainly distributed between 60°N  
572 and the equator, peaking concentrations of BC and OC as shown in Figs. 9 and 10 are located  
573 near the tropics in the biomass burning regions (e.g., the maritime continent, Central Africa,  
574 South America), and their seasonal variations from DJF to JJA are evidently weaker than  
575 those of sulfate except in South America. In boreal summer, there are centers of high values  
576 in the industrial regions in the Northern Hemisphere mid-latitudes (i.e., East Asia, South Asia,  
577 Europe, and North America). These main features of spatial and seasonal variations in CMIP5  
578 data are well captured by BCC-ESM1, and the BCC-ESM1 vs. CMIP5 spatial correlation  
579 coefficients (Figure 13) are 0.90 (OC in DJF), 0.91 (BC in DJF), 0.91 (OC in JJA) and 0.92  
580 (BC in JJA). There are less deviations of spatial pattern for OC in DJF and JJA, but larger  
581 deviation for BC from CMIP5 data (Figure 13).

582 As show in Figure 11, dust concentrations in the atmosphere show largest values over  
583 strong source regions such as Northern Africa, Southwest and Central Asia, and Australia,

584 and over their outflow regions such as the Atlantic and the western Pacific. In DJF, the  
585 CMIP5 data shows centers of high concentrations over East Asia and Central North America,  
586 but both centers are missing in BCC-ESM1. However, these two high-value centers in the  
587 CMIP5 data may not be true, since frozen soils in these areas in winter lead to unfavorable  
588 conditions for soil erosion by winds. The spatial correlation coefficients between CMIP5 and  
589 BCC-ESM1 remain high: 0.95 in JJA and 0.88 in DJF (Figure 13). Small deviations of spatial  
590 pattern for dust simulations in BCC-ESM1 show less magnitude of dust maximums against  
591 with CMIP5 data (Figure 13).

592 As shown in Figure 12, high sea salt concentrations are generally over the storm track  
593 regions over the oceans, e.g., mid-latitudes in the Northern Oceans in DJF and the Southern  
594 Ocean in JJA where wind speeds and thus sea salt emissions are higher. In addition, there is a  
595 belt of high sea salt concentrations in the subtropics of both hemispheres where precipitation  
596 scavenging is weak. Their spatial distributions in BCC-ESM1 are consistent with the CMIP5  
597 data with correlation coefficients of 0.92 in JJA and 0.90 in DJF (Figure 13). The spatial  
598 deviations of sea salt are much closer to CMIP5 data than those of sulfate, OC, BC, and dust  
599 distributions (Figure 13).

600 Figure 14 shows vertical distributions of zonally-averaged annual mean concentrations  
601 of sulfate, organic carbon, black carbon, dust, and sea salt aerosols in the period of 1991-2000.  
602 Both BCC-ESM1 and CMIP5 results show that strong sulfur, OC, and BC emissions in the  
603 industrial regions of the Northern Hemisphere mid-latitudes can rise upward and be  
604 transported towards the North Pole in the mid- to upper troposphere. Most of OC, BC, and  
605 dust aerosols are confined below 500 hPa, while sulfate can be transported to higher altitudes.  
606 Sea salt aerosols are mostly confined below 700 hPa, as the particles are large in size and  
607 favorable for wet removal and gravitational settling towards the surface. It can be seen that  
608 BCC-ESM1 tends to simulate less upward transport of aerosols than the CMIP5 data, likely  
609 reflecting the omission of deep convection transport of tracers in BCC-ESM1.

610 The CMIP5 data used here are mainly from model simulations. We will further evaluate  
611 the BCC-ESM1 model results with ground observations. Annual mean  $\text{SO}_4^{2-}$ , BC and OC  
612 aerosol observations from the Interagency Monitoring of Protected Visual Environments  
613 (IMPROVE) sites over 1990-2005 in the United States

614 (<http://vista.cira.colostate.edu/IMPROVE/>) and from the European Monitoring and Evaluation  
615 Programme (EMEP) (<http://www.emep.int>) sites over 1995-2005 are used. As shown in  
616 Figure 15a and 15b, the BCC-ESM simulated sulfate concentrations are in general  
617 comparable to the EMEP observations in Europe, but are systematically by about  $1 \mu\text{g m}^{-3}$   
618 higher than the U.S. IMPROVE observations. As for BC, there are large model biases at both  
619 European and U.S. sites (Figs. 15c and 15d), especially BCC-ESM overestimates BC  
620 concentrations at the IMPROVE sites. The observed OC concentrations are slightly  
621 overestimated for IMPROVE sites but systematically underestimated for EMEP sites. Some  
622 statistical features for simulated concentrations versus EMEP and IMPROVE observations are  
623 listed in Table 7. These comparisons are overall fairly reasonable considering the  
624 uncertainties in emissions and the coarse model resolution.

625 We then evaluate the simulated BC concentrations from BCC-ESM1 with the HIAPER  
626 (High-Performance Instrumented Airborne Platform for Environmental Research)  
627 Pole-to-Pole Observations (HIPPO) (Wofsy et al., 2011). The HIPPO campaign provided  
628 observations of black carbon concentration profiles over Pacific Ocean and North America  
629 between 2009 and 2011. Following Tilmes et al. (2016), model results here are sampled along  
630 the HIPPO flight tracks and then averaged to different latitude and altitude bands for  
631 comparison. As shown in Figure 16, BCC-ESM1 and HIPPO aircraft observations shows  
632 reasonable agreement in terms of the spatial distributions and seasonal variations of BC levels.  
633 BCC-ESM1 generally reproduces the observed hemispheric gradients of BC, i.e. the larger  
634 burden in the NH compared to the SH, in consistent with Figures 10 and 14. The model shows  
635 large overestimations of BC observations over the tropics, which is also found in the  
636 CAM4-chem global chemical model (Tilmes et al., 2016).

#### 637 **4.4 Aerosol Optical Properties**

638 Aerosol optical depth (AOD) is an indicator of the reduction in incoming solar  
639 radiation (at a particular wavelength) due to scattering and absorption of sunlight by aerosols.  
640 In this study, we calculate the AOD at 550 nm for all aerosols including sulfate, BC, organic  
641 carbon, sea salt and dust as the product of aerosol dry mass concentrations, aerosol water  
642 content, and their specific extinction coefficients. The total AOD is calculated by summing

643 the AOD in each model layer for each aerosol species using the assumption that they are  
644 externally mixed. The AOD observations retrieved from MODIS and MISR over the period of  
645 1997-2003, and from AERONET over the period of 1998–2005 (<http://aeronet.gsfc.nasa.gov>)  
646 are used to evaluate the averaged AOD at 550 nm in BCC-ESM. Figure 17 shows averages of  
647 MISR and MODIS AOD with corresponding averages from BCC-ESM. The BCC-ESM1  
648 simulated AOD generally captures the spatial distribution of MISR and MODIS retrievals.  
649 The model overestimates AOD over East China. It also systematically underestimates the  
650 MODIS observations in the Southern Hemisphere, but is closer to MISR observations. Figure  
651 18 shows multi-years annual means of BCC-ESM1 simulated AOD values versus  
652 observations from AERONET over the period of 1998–2005. The basic pattern of modeled  
653 global AOD is similar to that of observations and their spatial correlation reaches 0.56. Large  
654 values of AOD are mainly distributed in land continents such as North African, South Asia,  
655 East Asia, Europe, and eastern part of North America. Figures 19a-19d present scatter plots of  
656 observed versus simulated multi-year monthly mean AOD at those sites of AERONET in  
657 Europe, North America, East Asia, and South Asia over the period of 1998-2005, respectively.  
658 Model simulated monthly AOD generally agrees with observations within a factor of 2 for  
659 most sites. BCC-ESM slightly overestimates the AOD in European and North American sites.  
660 In those regions, BCC-ESM also slightly overestimates MODIS and MISR AOD observations  
661 (Fig. 17).

## 662 **5. Summary and discussions**

663 This paper presents a primary evaluation of aerosols simulated in version 1 of the Beijing  
664 Climate Center Earth System Model (BCC-ESM1) with the implementation of the interactive  
665 atmospheric chemistry and aerosol based on the newly developed BCC-CSM2. Global  
666 aerosols (including sulfate, organic carbon, black carbon, dust and sea salt) and major  
667 greenhouse gases (e.g., O<sub>3</sub>, CH<sub>4</sub>, N<sub>2</sub>O) in the atmosphere can be interactively simulated when  
668 anthropogenic emissions are provided to the model. Concentrations of all aerosols in  
669 BCC-ESM1 are determined by the processes of advective transport, emission, gas-phase  
670 chemical reactions, dry deposition, gravitational settling, and wet scavenging by clouds and  
671 precipitation. The nucleation and coagulation of aerosols are ignored in the present version of  
672 BCC-ESM1. Effects of aerosols on radiation, cloud, and precipitation are fully included.

673 We evaluate the performance of BCC-ESM1 in simulating aerosols and their optical  
674 properties in the 20th century following CMIP6 historical simulation according to the  
675 requirement of the AerChemMIP. It is forced with anthropogenic emissions evolving from  
676 1850 to 2014 but some WMGHGs such as CH<sub>4</sub>, N<sub>2</sub>O, CO<sub>2</sub>, CFC11 and CFC12 are prescribed  
677 using CMIP6 prescribed concentrations (to replace prognostic values of CH<sub>4</sub> and N<sub>2</sub>O from  
678 the chemistry scheme). Both direct and indirect effects of aerosols are considered in  
679 BCC-ESM1. Initial conditions of the CMIP6 historical simulation are obtained from a  
680 600-year piControl simulation in the absence of anthropogenic emissions, which well captures  
681 the pre-industrial concentrations of SO<sub>4</sub><sup>2-</sup>, organic carbon (OC), black carbon (BC), dust, and  
682 sea salt aerosols and are consistent with the CMIP5 recommended concentrations for the year  
683 1850. With the CMIP6 anthropogenic emissions of SO<sub>2</sub>, OC, and BC from 1850 to 2014 and  
684 their natural emissions implemented in BCC-ESM1, the model simulated SO<sub>4</sub><sup>2-</sup>, BC, and OC  
685 aerosols in the atmosphere are highly correlated with the CMIP5-recommended data. The  
686 long-term trends of CMIP5 aerosols from 1850 to 2000 are also well simulated by  
687 BCC-ESM1. Global budgets of aerosols were evaluated through comparisons of BCC-ESM1  
688 results for 1990-2000 with reports in various literatures for sulfate, BC, OC, sea salt, and dust.  
689 Their annual total emissions, atmospheric mass loading, and mean lifetimes are all within the  
690 range of values reported in relevant literature. Evaluations of the spatial and vertical  
691 distributions of BCC-ESM1 simulated present-day SO<sub>4</sub><sup>2-</sup>, OC, BC, Dust, and sea salt aerosol  
692 concentrations against the CMIP5 datasets and in-situ measurements of surface networks  
693 (IMPROVE in the U.S. and EMEP in Europe), and HIPPO aircraft observations indicate good  
694 agreement among them. The BCC-ESM1 simulates weaker upward transport of aerosols from  
695 the surface to the middle and upper troposphere (with reference to CMIP5-recommended  
696 data), likely reflecting a lack of deep convection transport of chemical species in the present  
697 version of BCC-ESM1. The AOD at 550 nm for all aerosols including sulfate, BC, OC, sea  
698 salt, and dust aerosols was further compared with the satellite AOD observations retrieved  
699 from MODIS and MISR and surface AOD observations from AERONET. The BCC-ESM1  
700 model results are overall in good agreement with these observations within a factor of 2. All  
701 these comparisons demonstrate the success of the implementation of interactive aerosol and  
702 atmospheric chemistry in BCC-ESM1.



703 This work has only evaluated the ability of BCC-ESM1 to simulate aerosols. The  
704 variations of aerosols especially for sulfate are related to other gaseous tracers such as OH  
705 and NO<sub>3</sub> (Table 2), which are determined by the MOZART2 gaseous chemical scheme as  
706 implemented in BCC-ESM1, and require further evaluation. As limited length of the text, the  
707 other optical feature of aerosols such as extinction coefficients, single scattering albedo and  
708 asymmetry parameters, and even their feedbacks on radiation and global temperature change  
709 will be explored in the other paper. O<sub>3</sub> is evaluated in this work. Other GHGs such as CH<sub>4</sub> and  
710 N<sub>2</sub>O concentrations can be simulated when forced with emissions and their simulations also  
711 need to be evaluated in future.

## 712 **6. Code and data availability**

713 Source codes of BCC-ESM1 model are freely available upon request addressed to  
714 Tongwen Wu (twwu@cma.gov.cn). Model output of BCC CMIP6 AerChemMIP simulations  
715 described in this paper is distributed through ESGF and freely accessible through the ESGF  
716 data portals after registration. Details about ESGF are presented on the CMIP Panel website at  
717 <http://www.wcrp-climate.org/index.php/wgcm-cmip/about-cmip>.

718

## 719 **Author contributions**

720 Tongwen Wu led the BCC-ESM1 development. All other co-authors have contributions  
721 to it. Fang Zhang and Jie Zhang designed the experiments and carried them out. Tongwen Wu,  
722 Laurent Li, Lin Zhang, Xiaohong Liu, Aixue Hu, and Jun Wang wrote the final document  
723 with contributions from all other authors.

724

## 725 **Acknowledgements**

726 This work was supported by The National Key Research and Development Program of China  
727 (2016YFA0602100). All the figures are created by the NCAR Command Language (Version  
728 6.6.2) [Software].

729

## 730 **References**

731 Albani, S., Mahowald, N. M., Perry, A. T., Scanza, R. A., Zender, C. S., Heavens, N. G.,  
732 Maggi, V., Kok, J. F., and Otto-Bliesner, B. L.: Improved dust representation in the

733 Community Atmosphere Model, *J. Adv. Model. Earth Syst.*, 6, 541–570,  
734 doi:10.1002/2013MS000279, 2014.

735 Albrecht, B.: Aerosols, cloud microphysics, and fractional cloudiness, *Science*, 245, 1227–  
736 1230, 1989.

737 Arora, V., Boer, G., Friedlingstein, P., Eby, M., Jones, C., Christian, J., Bonan, G., Bopp, L.,  
738 Brovkin, V., Cadule, P., Hajima, T., Ilyina, T., Lindsay, K., Tjiputra, J., and Wu, T.:  
739 Carbon-concentration and carbon-climate feedbacks in CMIP5 Earth system models. *J.*  
740 *Climate*, 26, 5289–5314, 2013.

741 Austin, J., Butchart, N., and Shine, K. P.: Possibility of an Arctic ozone hole in a  
742 doubled-CO<sub>2</sub> climate, *Nature*, 360, 221–225, 1992

743 Barth, M.C., Rasch, P.J., Kiehl, J.T., Benkowitz, C.M., and Schwartz, S.E.: Sulfur chemistry  
744 in the National Center for Atmospheric Research Community Climate Model:  
745 Description, evaluation, features, and sensitivity to aqueous chemistry. *J. Geophys. Res.*,  
746 105, D1, 1387-1415, 2000.

747 Bey I., Jacob, D. J., Yantosca, R. M., Logan, J. A., Field, B., Fiore, A. M., Li, Q., Liu, H.,  
748 Mickley, L. J., and Schultz, M.: Global modeling of tropospheric chemistry with  
749 assimilated meteorology: Model description and evaluation, *J. Geophys. Res.*, 106,  
750 23,073-23,096, 2001

751 Boucher, O., Lohmann, U.: The sulphate-CCN-cloud albedo effect – a sensitivity study with  
752 two general circulation models, *Tellus* 47B, 281–300, 1995.

753 Brasseur, G. P., Hauglustaine, D. A., Walters, S., Rasch, P. J., Müller, J.-F., Granier, C., and  
754 Tie, X. X.: MOZART, a global chemical transport model for ozone and related chemical  
755 tracers: 1. Model description, *J. Geophys. Res.*, 103, 28,265– 28,289, 1998.

756 Brasseur, G. P., Tie, X. X., Rasch, P. J., and Lefèvre, F.: A three - dimensional simulation of  
757 the Antarctic ozone hole: Impact of anthropogenic chlorine on the lower stratosphere and  
758 upper troposphere, *J. Geophys. Res.*, 102, 8909–8930, 1997.

759 Cariolle, D., Lasserre-Bigorry, A., and Royer, J.-F.: A general circulation model simulation of  
760 the springtime Antarctic ozone decrease and its impact on midlatitudes, *J. Geophys. Res.*,  
761 95, 1883–1898, 1990.

762 Chen, C., and Cotton, W. R.: The physics of the marine stratocumulus-capped mixed layer, *J.*  
763 *Atmos. Sci.*, 44 (50), 2951–2977, 1987.

764 Chin, M., Ginoux, P., Kinne, S., Torres, O., Holben, B.N., Duncan, B.N., Martin, R.V., Logan, J.A.,

765 Higurashi, A., Naka-jima, T.: Tropospheric aerosol optical thickness from the GOCART  
766 model and comparisons with satellite and Sun photometer measurements. *J. Atmos.*  
767 *Sci.* 59:461–483, 2002.

768 Chuang, C. C., Penner, J. E., Taylor, K. E., Grossman, A. S., and Walton, J. J.: An assessment  
769 of the radiative effects of anthropogenic sulfate, *J. Geophys. Res.*, 102, 3761–3778,  
770 1997.

771 Collins, W. J., Lamarque, J.-F., Schulz, M., Boucher, O., Eyring, V., Hegglin, M. I.,  
772 Maycock, A., Myhre, G., Prather, M., Shindell, D., Smith, S. J.: AerChemMIP:  
773 quantifying the effects of chemistry and aerosols in CMIP6, *Geosci. Model Dev.*, 10,  
774 585–607, 2017.

775 Collins, W. D., Rasch, P. J., Boville, B. A., Hack, J. J., McCaa, J. R., Williamson, D. L.,  
776 Kiehl, J. T., Briegleb, B. P., Bitz, C., Lin, S.-J., Zhang, M., and Dai, Y.: Description of  
777 the NCAR Community Atmosphere Model (CAM3). *Nat. Cent. for Atmos. Res.*,  
778 Boulder, Colo., 2004.

779 Cooke, W.F., Wilson, J.J.N.: A global black carbon aerosol model. *J. Geophys. Res. Atmos.*  
780 101, 19395–19409, 1996.

781 Cunnold, D., Alyea, F., Phillips, N., Prinn, R.: A three-dimensional dynamical-chemical  
782 model of atmospheric ozone, *J. Atmos. Sci.*, 32, 170-194, 1975.

783 Dentener, F., Kinne, S., Bond, T., Boucher, O., Cofala, J., Generoso, S., Ginoux, P., Gong, S.,  
784 Hoelzemann, J. J., Ito, A., Marelli, L., Penner, J. E., Putaud, J.-P., Textor, C., Schulz, M.,  
785 van der Werf, G. R., and Wilson, J.: Emissions of primary aerosol and precursor gases in  
786 the years 2000 and 1750 prescribed data-sets for AeroCom, *Atmos. Chem. Phys.*, 6,  
787 4321–4344, doi:10.5194/acp-6-4321-2006, 2006.

788 Eyring, V., Bony, S., Meehl, G. A., Senior, C. A., Stevens, B., Stouffer, R. J., and Taylor, K.  
789 E.: Overview of the Coupled Model Intercomparison Project Phase 6 (CMIP6)  
790 experimental design and organization, *Geosci. Model Dev.*, 9, 1937–1958,  
791 doi:10.5194/gmd-9-1937-2016, 2016.

792 Feichter, J., Kjellstrom, E., Rodhe, H., Dentener, F., Lelieveld, J., Roelofs, G.-J.: Simulation  
793 of the tropospheric sulfur cycle in a global climate model, 30: 1693-1707, 1996.

794 Ghan, S. J. and Easter, R. C.: Impact of cloud-borne aerosol representation on aerosol direct  
795 and indirect effects, *Atmos. Chem. Phys.*, 6, 4163–4174, 2006.

796 Ginoux, P., M. Chin, I. Tegen, J. M. Prospero, B. Holben, O. Dubovik, and S.-J. Lin (2001),

797 Sources and distributions of dust aerosols simulated with the GOCART model, J.  
798 Geophys. Res., 106, 20,255 – 20,274.

799 Giorgi, F., and Chameides, W. L.: The rainout parameterization in a photochemical model, J.  
800 Geophys. Res., 90, 7872–7880, 1985.

801 Guenther, A. B., Jiang, X., Heald, C. L., et al.: The Model of Emissions of Gases and  
802 Aerosols from Nature Version 2.1 (MEGAN2.1): An Extended and Updated Framework  
803 for Modeling Biogenic Emissions. *Geoscientific Model Development* 5(6): 1471–1492,  
804 2012.

805 Guenther, A., Baugh, B. Brasseur, G., Greenberg, J., Harley, P., Klinger, L., Serca, D., and  
806 Vierling, L.: Isoprene emission estimates and uncertainties for the Central African  
807 EXPRESSO study domain, *J. Geophys. Res.*, 104(D23), 30,625–30,639, 1999.

808 Hoesly, R. M., Smith, S. ., Feng, L., Klimont, Z., Janssens-Maenhout, G., Pitkanen, T.,  
809 Seibert, J. J., Vu, L., Andres, R. J., Bolt, R. M., Bond, T. C., Dawidowski, L., Kholod, N.,  
810 Kurokawa, J., Li, M., Liu, L., Lu, Z., Moura, M. C. P., O'Rourke, R. R., and Zhang Q.:  
811 Historical (1750–2014) anthropogenic emissions of reactive gases and aerosols from the  
812 Community Emission Data System (CEDS), *Geosci. Model Dev.*, 11, 369-408, 2018

813 Horowitz, L.W., Walters, S., Mauzerall, D. L., Emmons, L. K., Rasch, P. J., Granier, C., Tie,  
814 X., Lamarque, J.-F., Schultz, M. G., Tyndall, G. S., Orlando, J. J., Brasseur, G. P.: A  
815 global simulation of tropospheric ozone and related tracers: Description and evaluation  
816 of MOZART, version 2, *J. Geophys. Res.*, 108(D24), 4784, doi:10.1029/2002JD002853,  
817 2003.

818 Horowitz, L. W.: Past, present, and future concentrations of tropospheric ozone and aerosols:  
819 Methodology, ozone evaluation, and sensitivity to aerosol wet removal, *J. Geophys. Res.*,  
820 111, D22211, doi:10.1029/2005JD006937, 2006.

821 Hoffman, F. M., Randerson, J. T., Arora, V. K., Bao, Q., Cadule, P., Ji, D., Jones, C. D.,  
822 Kawamiya, M., Khatiwala, S., Lindsay, K., Obata, A., Shevliakova, E., Six, K. D.,  
823 Tjiputra, J. F., Volodin, E. M., and Wu, T.: Causes and implications of persistent  
824 atmospheric carbon dioxide biases in Earth System Models, *J. Geophys. Res. Biogeosci.*,  
825 119, 141–162, doi:10.1002/2013JG002381, 2014.

826 Holtslag, A. A. M., and Boville, B. A.: Local versus nonlocal boundary-layer diffusion in a  
827 global climate model, *J. Climate*, 6, 1825–1842, 1993.

828 Jacobson, M.Z.: Investigating cloud absorption effects: global absorption properties of black

829 carbon, tar balls, and soil dust in clouds and aerosols. *J. Geophys. Res.* 117, D06205,  
830 2012.

831 Jones, C.D., Arora, V., Friedlingstein, P., Bopp, L., Brovkin, V., Dunne, J., Graven, H.,  
832 Hoffman, F., Ilyina, T., John, J. G., Jung, M., Kawamiya, M., Koven, C., Pongratz, J.,  
833 Raddatz, T., Randerson, J. T., and Zaehle, S.: C4MIP – The Coupled Climate–Carbon  
834 Cycle Model Intercomparison Project: experimental protocol for CMIP6, *Geosci. Model*  
835 *Dev.*, 9, 2853–2880, doi:10.5194/gmd-9-2853-2016, 2016.

836 Lamarque, J.-F., Shindell, D. T., Josse, B., Young, P. J., Cionni, I., Eyring, V., Bergmann, D.,  
837 Cameron-Smith, P., Collins, W. J., Doherty, R., Dalsoren, S., Faluvegi, G., Folberth, G.,  
838 Ghan, S. J., Horowitz, L. W., Lee, Y. H., MacKenzie, I. A., Nagashima, T., Naik, V.,  
839 Plummer, D., Righi, M., Rumbold, S. T., Schulz, M., Skeie, R. B., Stevenson, D. S.,  
840 Strode, S., Sudo, K., Szopa, S., Voulgarakis, A., and Zeng, G.: The Atmospheric  
841 Chemistry and Climate Model Intercomparison Project (ACCMIP): overview and  
842 description of models, simulations and climate diagnostics, *Geosci. Model Dev.*, 6, 179–  
843 206, doi:10.5194/gmd-6-179-2013, 2013.

844 Lamarque, J.-F., Emmons, L. K., Hess, P. G., Kinnison, D. E., Tilmes, S., Vitt, F., Heald, C.  
845 L., Holland, E. A., Lauritzen, P. H., Neu, J., Orlando, J. J., Rasch, P. J., and Tyndall, G.  
846 K.: CAM-chem: description and evaluation of interactive atmospheric chemistry in the  
847 Community Earth System Model, *Geosci. Model Dev.*, 5, 369–411, 2012

848 Lamarque, J.-F., Bond, T. C., Eyring, V., Granier, C., Heil, A., Klimont, Z., Lee, D., Liousse,  
849 C., Mieville, A., Owen, B., Schultz, M. G., Shindell, D., Smith, S. J., Stehfest, E., Van  
850 Aardenne, J., Cooper, O. R., Kainuma, M., Mahowald, N., McConnell, J. R., Naik, V.,  
851 Riahi, K., and van Vuuren, D. P.: Historical (1850–2000) gridded anthropogenic and  
852 biomass burning emissions of reactive gases and aerosols: methodology and application,  
853 *Atmos. Chem. Phys.*, 10, 7017–7039, <https://doi.org/10.5194/acp-10-7017-2010>, 2010.

854 Lohmann, U., Feichter, J., Penner, J. E., and Leaitch, W. R.: Indirect effect of sulfate and  
855 carbonaceous aerosols: A mechanistic treatment. *J. Geophys. Res.*, 105, 12193–12206,  
856 2000

857 Li, W., Zhang, Y., Shi, X., Zhou, W., Huang, A., Mu, M., Qiu, B., Ji, J.: Development of the  
858 Land Surface Model BCC\_AVIM2.0 and Its Preliminary Performance in  
859 LS3MIP/CMIP6, *J. Meteor. Res.*, 33(5), doi: 10.1007/s13351-019-9016-y, 2019.

860 Liu, X. H., Penner, J. E., and Herzog, M.: Global modeling of aerosol dynamics: Model

861 description, evaluation, and interactions between sulfate and nonsulfate aerosols, J.  
862 Geophys. Res.-Atmos., 110, D18206, doi:10.1029/2004jd005674, 2005.

863 Liu, X., Easter, R.C. Ghan, S.J., Zaveri, R., Rasch, P., Shi, X., Lamarque, J.-F., Gettelman, A.,  
864 Morrison, H., Vitt, F., Conley, A., Park, S., Neale, R., Hannay, C., Ekman, A.M., Hess,  
865 P., Mahowald, N., Collins, W., Iacono, M.J., Bretherton, C.S., Flanner, M.G., and  
866 Mitchell, D.: Toward a Minimal Representation of Aerosols in Climate Models:  
867 Description and Evaluation in the Community Atmosphere Model CAM5.  
868 Geos.Model.Dev. 5(3):709-739. 2012.

869 Liu, X., Ma, P. -L., Wang, H., Tilmes, S., Singh, B., Easter, R. C., Ghan, S. J., and Rasch, P.  
870 J.: Description and evaluation of a new four-mode version of the Modal Aerosol Module  
871 (MAM4) within version 5.3 of the Community Atmosphere Model, Geosci. Model Dev.,  
872 9, 505–522, <https://doi.org/10.5194/gmd-9-505-2016>, 2016.

873 Liu, J., Mauzerall, D.L., Horowitz, L.W., Ginoux, P., Fiore, A.M.: Evaluation intercontinental  
874 transport of fine aerosols: (1) methodology, global aerosol distribution and optical depth.  
875 Atmos Environ 43:4327–4338, 2009.

876 Lu, X., Zhang, L., Wu, T., Long, M., Wang, J., Jacob, D., Zhang F., Zhang, J., Eastham, S.,  
877 Hu, L., Zhu, L., Liu, X., an Wei, M.: Development of the global atmospheric general  
878 circulation-chemistry model BCC-GEOS-Chem v1.0: model description and evaluation,  
879 submitted to Geos.Model.Dev.

880 Mahowald, N., Lamarque, J.-F., Tie, X., and Wolff, E.: Sea salt aerosol response to climate  
881 change: last glacial maximum, preindustrial and doubled carbon dioxide climates, J.  
882 Geophys. Res., 111, D05303, doi:10.1029/2005JD006459, 2006.

883 Martin, R. V., et al.: Interpretation of TOMS observations of tropical tropospheric ozone with  
884 a global model and in situ observations, J. Geophys. Res., 107(D18), 4351,  
885 doi:10.1029/2001JD001480, 2002.

886 Matsui, H., and Mahowald, N.: Development of a global aerosol model using a  
887 two-dimensional sectional method: 2. Evaluation and sensitivity simulations, J. Adv.  
888 Model. Earth Syst., 9, 1887 – 1920, doi:10.1002/2017MS000937, 2017.

889 Mora, C., Wei, C.-L., Rollo, A., Amaro, T., Baco, A.R., Billett, D., Bopp, L., Chen, Q.,  
890 Collier, M., Danovaro, R., Gooday, A.J., Grube, B.M., Halloran, P.R., Ingels, J., Jones,  
891 D.O.B., Levin, L.A., Nakano, H., Norling, K., Ramirez-Llodra, E., Rex, M., Ruh, H.A.,  
892 Smith, C.R., Sweetman, A.K., Thurber, A.R., Tjiputra, J. F., Usseglio, P., Watling, L.,

893 Wu, T., Yasuhara, M.: Biotic and human vulnerability to projected ocean  
894 biogeochemistry change over the 21st century, *PLoS Biol* 11(10): e1001682.  
895 doi:10.1371/journal.pbio.1001682, 2013.

896 NCAR Command Language (Version 6.6.2) [Software], Boulder, Colorado:  
897 UCAR/NCAR/CISL/TDD. <http://dx.doi.org/10.5065/D6WD3XH5>, 2019.

898 Neale, R. B., et al.: Description of the NCAR Community Atmosphere Model (CAM 4.0),  
899 NCAR Tech. Note, TN-485, pp. 212, Natl. Cent. for Atmos. Res., Boulder, Colo., 2010

900 Neu, J. L. and Prather, M. J.: Toward a more physical representation of precipitation  
901 scavenging in global chemistry models: cloud overlap and ice physics and their impact  
902 on tropospheric ozone, *Atmos. Chem. Phys. Discuss.*, 11, 24413–24466,  
903 doi:10.5194/acpd-11-24413-2011, 2011.

904 Olivier, J.G.J., Bouwman, A.F., Van der Maas, C.W.M., Berdowski, J.J.M., Veldt, C., Bloos,  
905 J.P.J., Visschedijk, A.J.H., Zandveld, P.Y.J., Haverslag, J.L., Description of EDGAR  
906 Version 2.0: A set of global emission inventories of greenhouse gases and ozone  
907 depleting substances for all anthropogenic and most natural sources on a per country  
908 basis and on 1° x 1° grid. RIVM Techn. Report nr. 771060002, TNO-MEP report nr.  
909 R96/119. Nat. Inst. Of Public Health and the Environment/ Netherlands Organisation for  
910 Applied Scientific Research, Bilthoven, 1996.

911 Peng, Y., and Lohmann, U.: Sensitivity study of the spectral dispersion of the cloud droplet  
912 size distribution on the indirect aerosol effect, *Geophys. Res. Lett.*, 30(10), 1507,  
913 doi:10.1029/2003GL017192, 2003.

914 Price, C., and Rind, D.: A simple lightning parameterization for calculating global lightning  
915 distributions, *J. Geophys. Res.*, 97, 9919-9933, 1992.

916 Quaas, J., Boucher, O., and Lohmann, U.: Constraining the total aerosol indirect effect in  
917 the LMDZ and ECHAM4 GCMs using MODIS satellite data. *Atmos Chem Phys* 6,947–  
918 955, 2006.

919 Sander, S., Friedl, R. R., Ravishankara, A. R., et al.: Chemical Kinetics and Photochemical  
920 Data for Use in Atmospheric Studies, Evaluation Number 14, JPL Publication 02-25,  
921 NASA, Jet Propulsion Laboratory, California Institute of Technology, Pasadena, CA,  
922 2003.

923 Schlesinger, M. E., Mintz, Y.: Numerical simulation of ozone production, transport and

924 distribution with a global atmospheric general circulation model, *J.Atmos.Sci.*, 36:  
925 1325-1361, 1979.

926 Shindell, D.T., Horowitz, L.W., Schwarzkopf, M.D.: Composition Models in Climate  
927 Projections Based on Emissions Scenarios for Long-Lived and Short-Lived Radiatively  
928 Active Gases and Aerosols. H.Levy II, D.T. Shindell, A.Gilliland, M.D.Schwarzkopf,  
929 L.W.Horowitz, (eds.) .A Report by the U.S.Climate Change Science Program and the  
930 Subcommittee on Global Change Research, Washington, D.C., 2008

931 Solomon, S.: Stratospheric ozone depletion: A review of concepts and history, *Reviews of*  
932 *Geophysics*, 37, 275–316, 1999.

933 Taylor, K.E., Stouffer, R. J., Meehl, G. A.: An overview of CMIP5 and the experiment design,  
934 *Bull. Am. Meteorol. Soc.* 93, 485-498, 2012.

935 Tegen, I., Neubauer, D., Ferrachat, S., Siegenthaler-Le Drian, C., Bey, I., Schutgens, N., Stier,  
936 P., Watson-Parris, D., Stanelle, T., Schmidt, H., Rast, S., Kokkola, H., Schultz, M.,  
937 Schroeder, S., Daskalakis, N., Barthel, S., Heinold, B., and Lohmann, U.: The global  
938 aerosol–climate model ECHAM6.3–HAM2.3 – Part 1: Aerosol evaluation, *Geosci.*  
939 *Model Dev.*, 12, 1643–1677, <https://doi.org/10.5194/gmd-12-1643-2019>, 2019.

940 Textor, C., Schulz, M., Guibert, S., Kinne, S., Balkanski, Y., Bauer, S., Berntsen, T., Berglen,  
941 T., Boucher, O., Chin, M., Dentener, F., Diehl, T., Easter, R., Feichter, H., Fillmore, D.,  
942 Ghan, S., Ginoux, P., Gong, S., Grini, A., Hendricks, J., Horowitz, L., Huang, P., Isaksen,  
943 I., Iversen, I., Kloster, S., Koch, D., Kirkevåg, A., Kristjansson, J. E., Krol, M., Lauer, A.,  
944 Lamarque, J. F., Liu, X., Montanaro, V., Myhre, G., Penner, J., Pitari, G., Reddy, S.,  
945 Seland, Ø., Stier, P., Takemura, T., and Tie, X.: Analysis and quantification of the  
946 diversities of aerosol life cycles within AeroCom, *Atmos. Chem. Phys.*, 6, 1777–1813,  
947 <https://doi.org/10.5194/acp-6-1777-2006>, 2006.

948 Thomason, L. W., Ernest, N., Millán, L., Rieger, L., Bourassa, A., Vernier, J. P., Manney, G.,  
949 Luo, B.P., Arfeuille, F., Peter, T.: A global space - based stratospheric aerosol  
950 climatology: 1979-2016. *Earth System Science Data*, 10(1), 469–492, doi:  
951 10.5194/essd-10-469-2018, 2018.

952 Tie, X., Brasseur, G., Emmons, L., Horowitz, L., and Kinnison, D.: Effects of aerosols on  
953 tropospheric oxidants: A global model study, *J. Geophys. Res.*, 106, 2931– 2964, 2001.

954 Tie, X., Madronich, S., Walters, S., Edwards, D., Ginoux, P., Mahowald, N., Zhang, R., Luo,  
955 C., and Brasseur, G.: Assessment of the global impact of aerosols on tropospheric



956 oxidants, *J. Geophys. Res.*, 110, D03204, doi:10.1029/2004JD005359, 2005.

957 Tilmes, S., Lamarque, J.-F., Emmons, L. K., Kinnison, D. E., Marsh, D., Garcia, R. R., Smith,  
958 A. K., Neely, R. R., Conley, A., Vitt, F., Val Martin, M., Tanimoto, H., Simpson, I.,  
959 Blake, D. R., and Blake, N.: Representation of the Community Earth System Model  
960 (CESM1) CAM4-chem within the Chemistry-Climate Model Initiative (CCMI),  
961 *Geoscientific Model Development*, 9, 1853-1890, 2016.

962 Todd-Brown, K.E.O., Randerson, J.T., Hopkins, F., Arora, V., Hajima, T., Jones, C.,  
963 Shevliakova, E., Tjiputra, J., Volodin, E., Wu, T., Zhang, Q., Allison, S.D.: Changes in  
964 soil organic carbon storage predicted by Earth system models during the 21st century,  
965 *Biogeosciences*, 11, 2341-2356, 2014.

966 Wang, J., Hoffmann, A. A., Park, R., Jacob, D. J., and Martin, S. T.: Global distribution of  
967 solid and aqueous sulfate aerosols: effect of the hysteresis of particle phase transitions, *J.*  
968 *Geophys. Res.*, 113, D11206, Doi:11210.11029/12007JD009367, 2008a.

969 Wang, J., Jacob, D. J., and Martin, S. T.: Sensitivity of sulfate direct climate forcing to the  
970 hysteresis of particle phase transitions, *J. Geophys. Res.*, 113, D11207,  
971 doi:11210.11029/12007JD009368, 2008b.

972 Wesely, M. L.: Parameterization of surface resistance to gaseous dry deposition in  
973 regional-scale numerical models, *Atmos. Environ.*, 23, 1293–1304, 1989.

974 Wild, M., Folini, D., Schar, C., Loeb, N., Dutton, E.G., Konig-Langlo, G.: The global energy  
975 balance from a surface perspective, *Climate Dynamics*, 40: 3107-3134, 2013.

976 Williamson, D. L., and Rasch, P. J.: Two-dimensional semi-Lagrangian transport with  
977 shapepreserving interpolation, *Mon. Wea. Rev.*, 117, 102–129, 1989.

978 Wofsy, S. C. and the HIPPO team: HIAPER Pole-to-Pole Observations (HIPPO): fine-grained,  
979 global-scale measurements of climatically important atmospheric gases and aerosols,  
980 *Philos. T. R. Soc. A*, 369, 2073–86, doi:10.1098/rsta.2010.0313, 2011.

981 Wu, T., Song, L., Li, W., Wang, Z., Zhang, H., Xin, X., Zhang, Y., Zhang, L., Li, J., Wu, F.,  
982 Liu, Y., Zhang, F., Shi, X., Chu, M., Zhang, J., Fang, Y., Wang, F., Lu, Y., Liu, X., Wei,  
983 M., Liu, Q., Zhou, W., Dong, M., Zhao, Q., Ji, J., Li, L., Zhou, M.: An overview of BCC  
984 climate system model development and application for climate change studies. *J. Meteor.*  
985 *Res.*, 28(1), 34-56, 2014.

986 Wu, T., Li, W., Ji, J., Xin, X., Li, L., Wang, Z., Zhang, Y., Li, J., Zhang, F., Wei, M., Shi, X.,  
987 Wu, F., Zhang, L., Chu, M., Jie, W., Liu, Y., Wang, F., Liu, X., Li, Q., Dong, M., Liang,

988 X., Gao, Y., Zhang, J.: Global carbon budgets simulated by the Beijing climate center  
989 climate system model for the last century. *J Geophys Res Atmos*, 118, 4326-4347. doi:  
990 10.1002/jgrd.50320, 2013.

991 Wu, T., Lu, Y., Fang, Y., Xin, X., Li, L., Li, W., Jie, W., Zhang, J., Liu, Y., Zhang, L., Zhang,  
992 F., Zhang, Y., Wu, F., Li, J., Chu, M., Wang, Z., Shi, X., Liu, X., Wei, M., Huang, A.,  
993 Zhang, Y., and Liu, X.: The Beijing Climate Center Climate System Model (BCC-CSM):  
994 the main progress from CMIP5 to CMIP6, *Geos.Model Dev.*, 12, 1573-1600,  
995 <http://doi.org/10.5194/gmd-12-1573-2019>, 2019.

996 Young, P. J., Archibald, A. T., Bowman, K. W., Lamarque, J. F., Naik, V., Stevenson, D. S.,  
997 Tilmes, S., Voulgarakis, A., Wild, O., Bergmann, D., Cameron-Smith, P., Cionni, I.,  
998 Collins, W. J., Dalsøren, S. B., Doherty, R. M., Eyring, V., Faluvegi, G., Horowitz, L.  
999 W., Josse, B., Lee, Y. H., MacKenzie, I. A., Nagashima, T., Plummer, D. A., Righi, M.,  
1000 Rumbold, S. T., Skeie, R. B., Shindell, D. T., Strode, S. A., Sudo, K., Szopa, S., and  
1001 Zeng, G.: Pre-industrial to end 21st century projections of tropospheric ozone from the  
1002 Atmospheric Chemistry and Climate Model Intercomparison Project (ACCMIP), *Atmos.*  
1003 *Chem. Phys.*, 13, 2063-2090, <http://doi.org/10.5194/acp-13-2063-2013>, 2013.

1004 Young, P. J., Naik, V., Fiore, A. M., Gaudel, A., Guo, J., Lin, M. Y., Neu, J. L., Parrish, D. D.,  
1005 Rieder, H. E., Schnell, J. L., Tilmes, S., Wild, O., Zhang, L., Ziemke, J. R., Brandt, J.,  
1006 Delcloo, A., Doherty, R. M., Geels, C., Hegglin, M. I., Hu, L., Im, U., Kumar, R., Luhar,  
1007 A., Murray, L., Plummer, D., Rodriguez, J., Saiz-Lopez, A., Schultz, M. G., Woodhouse,  
1008 M. T., and Zeng, G.: Tropospheric Ozone Assessment Report: Assessment of  
1009 global-scale model performance for global and regional ozone distributions, variability,  
1010 and trends, *Elem Sci Anth*, 6, 10, <http://doi.org/10.1525/elementa.265>, 2018.

1011 Zender, C., Bian, H., and Newman, D.: Mineral Dust Entrainment and Deposition (DEAD)  
1012 model: Description and 1990s dust climatology, *J. Geophys. Res.*, 108(D14), 4416, doi:  
1013 10.1029/2002JD002775, 2003.

1014

1015 Table 1. Chemical species considered in BCC-AGCM3-Chem. Species marked with star (\*)  
 1016 denote those added in BCC-ESM1 apart from the 63 species used in MOZART2. In the  
 1017 column of surface emission, interactive surface emissions are considered for sea salt and dust.  
 1018

Species	Dry deposition	Wet deposition	Surface emission	Aircraft emission	Volcanic emission
O <sub>3</sub>	✓				
N <sub>2</sub> O			✓		
N					
NO	✓		✓	✓	
NO <sub>2</sub>	✓				
NO <sub>3</sub>					
HNO <sub>3</sub>	✓	✓			
HO <sub>2</sub> NO <sub>2</sub>	✓	✓			
N <sub>2</sub> O <sub>5</sub>					
CH <sub>4</sub>	✓		✓	✓	
CH <sub>3</sub> O <sub>2</sub>					
CH <sub>3</sub> OOH	✓	✓			
CH <sub>2</sub> O	✓	✓	✓		
CO	✓		✓	✓	
OH					
HO <sub>2</sub>					
H <sub>2</sub> O <sub>2</sub>	✓	✓			
C <sub>3</sub> H <sub>6</sub>			✓		
ISOP			✓		
Gas tracers					
PO <sub>2</sub>					
CH <sub>3</sub> CHO	✓	✓	✓		
POOH	✓	✓			
CH <sub>3</sub> CO <sub>3</sub>					
CH <sub>3</sub> COOOH	✓	✓			
PAN	✓				
ONIT	✓	✓			
C <sub>2</sub> H <sub>6</sub>			✓		
C <sub>2</sub> H <sub>4</sub>			✓		
C <sub>4</sub> H <sub>10</sub>			✓		
MPAN	✓				
ISOPO <sub>2</sub>					
MVK		✓			
MACR		✓			
MACRO <sub>2</sub>					
MACROOH	✓	✓			
MCO <sub>3</sub>					
C <sub>2</sub> H <sub>5</sub> O <sub>2</sub>					
C <sub>2</sub> H <sub>5</sub> OOH	✓	✓			
C <sub>10</sub> H <sub>16</sub>			✓		

1019

1020

Species name	Dry deposition	Wet deposition	Surface emission	Aircraft emission	Volcanic emission
C <sub>3</sub> H <sub>8</sub>			✓		
C <sub>3</sub> H <sub>7</sub> O <sub>2</sub>					
C <sub>3</sub> H <sub>7</sub> OOH	✓	✓			
CH <sub>3</sub> COCH <sub>3</sub>	✓		✓		
ROOH		✓			
CH <sub>3</sub> OH	✓	✓	✓		
C <sub>2</sub> H <sub>5</sub> OH	✓	✓	✓		
GLYALD	✓	✓			
HYAC	✓	✓			
EO <sub>2</sub>					
EO					
HYDRALD	✓	✓			
RO <sub>2</sub>					
CH <sub>3</sub> COCHO	✓	✓	✓		
Rn-222					
Pb-210	✓	✓			
ISOPNO <sub>3</sub>		✓			
ONITR	✓	✓			
XO <sub>2</sub>					
XOOH	✓	✓			
ISOPOOH	✓	✓			
H <sub>2</sub>	✓		✓		
Stratospheric O <sub>3</sub>	✓				
Inert O <sub>3</sub>	✓				
SO <sub>2</sub> *	✓	✓	✓	✓	✓
DMS*			✓		
NH <sub>3</sub> *			✓	✓	
SO <sub>4</sub> <sup>2-</sup> *	✓	✓			
OC1*	✓	✓	✓	✓	
OC2*	✓	✓	✓	✓	
BC1*	✓	✓	✓	✓	
BC2*	✓	✓	✓	✓	
SSLT01*	✓	✓			
SSLT02*	✓	✓			
SSLT03*	✓	✓			
SSLT04*	✓	✓			
DST01*	✓	✓			
DST02*	✓	✓			
DST03*	✓	✓			
DST04*	✓	✓			

1024 Table 2. Gas-phase chemical reactions for NH<sub>3</sub> and bulk aerosols precursors following  
 1025 CAM-Chem (Lamarque et al., 2012). The reaction rates (s<sup>-1</sup>) refer to Tie et al. (2001) and  
 1026 Sander et al. (2003), and Cooke and Wilson (1996). Temperature (T) is expressed in K, air  
 1027 density (M) in molecule cm<sup>-3</sup>, ki and ko in cm<sup>3</sup> molecule<sup>-1</sup> s<sup>-1</sup>.  
 1028

Chemical reactions	Rate
NH <sub>3</sub> + OH → H <sub>2</sub> O	1.70E-12*exp(-710/T)
SO <sub>2</sub> + OH → SO <sub>4</sub> <sup>2-</sup>	ko/(1.+ko*M/ki)*f**(1./(1.+log10(ko*M/ki))), in which ko=3.0E-31*(300/T)**3.3; ki=1.E-12; f=0.6
DMS + OH → SO <sub>2</sub>	9.60E-12*exp(-234./T)
DMS + OH → .5*SO <sub>2</sub> + .5*HO <sub>2</sub>	1.7E-42*exp(7810/T)*M*0.21/(1+5.5E-31*exp(7460/T)* M* 0.21)
DMS + NO <sub>3</sub> → SO <sub>2</sub> + HNO <sub>3</sub>	1.90E-13*exp( 520/T)
BC1 → BC2	7.10E-06
OC1 → OC2	7.10E-06

1029  
 1030

1031

1032

1033

Table 3. Size and density parameters of bulk aerosols.

Aerosols	Species Name	Mean radius ( $\mu\text{m}$ ) / bin size ( $\mu\text{m}$ )	Geometric standard deviation ( $\mu\text{m}$ )	Density ( $\text{g cm}^{-3}$ )
SO <sub>4</sub> <sup>2-</sup>	Sulfate	0.05	2.03	1.77
BC1	hydrophobic black carbon	0.02	2.00	1.0
BC2	hydrophilic black carbon	0.02	2.00	1.0
OC1	hydrophobic organic carbon	0.03	2.24	1.8
OC2	hydrophilic organic carbon	0.03	2.24	1.8
DST01	Dust	0.55 / bin: 0.1-1.0	2.00	2.5
DST02	Dust	1.75 / bin: 1.0-2.5	2.00	2.5
DST03	Dust	3.75 / bin: 2.5-5.0	2.00	2.5
DST04	Dust	7.50 / bin: 5.0-10.	2.00	2.5
SSLT01	Sea salt	0.52 / bin: 0.2-1.0	2.00	2.2
SSLT02	Sea salt	2.38 / bin: 1.0-3.0	2.00	2.2
SSLT03	Sea salt	4.86 / bin: 3.0-10.	2.00	2.2
SSLT04	Sea salt	15.14 / bin: 10.-20.	2.00	2.2

1034

Table 4. Source of emission data. MOZART2 data denote the standard tropospheric chemistry package for MOZART contains surface emissions from the EDGAR 2.0 data base (Olivier et al., 1996). ACCMIP data are downloaded from the IPCC ACCMIP emission inventory (<http://accent.aero.jussieu.fr/ACCMIP.php>) and they vary from 1850 to 2000, in 10-year steps (Lamarque et al., 2010). CMIP6 data are from <https://esgf-node.llnl.gov/search/input4mips/>. Anthropogenic emission includes Industrial and fossil fuel use, agriculture, ships, and etc. Biomass burning includes vegetation fires incl. fuel wood and agricultural burning.

Species	Anthropogenic emission	Biomass burning	Biogenic emissions from vegetation	Biogenic emissions from soil	Oceanic emissions	Airplane emission	Volcanic emission
C <sub>2</sub> H <sub>4</sub>	CMIP6	CMIP6	On-line computation		MOZART2		
C <sub>2</sub> H <sub>5</sub> OH	CMIP6	CMIP6					
C <sub>2</sub> H <sub>6</sub>	CMIP6	CMIP6	ACCMIP		MOZART2		
C <sub>3</sub> H <sub>6</sub>	CMIP6	CMIP6	On-line computation		MOZART2		
C <sub>3</sub> H <sub>8</sub>	CMIP6	CMIP6	ACCMIP		MOZART2		
C <sub>4</sub> H <sub>10</sub>	CMIP6	CMIP5	MOZART2		MOZART2		
CH <sub>2</sub> O	CMIP6	CMIP6					
CH <sub>3</sub> CHO	ACCMIP	CMIP6					
CH <sub>3</sub> COCHO		CMIP6					
CH <sub>3</sub> OH	ACCMIP	CMIP6	ACCMIP				
CH <sub>3</sub> COCH <sub>3</sub>	ACCMIP	ACCMIP	On-line computation		MOZART2		
ISOP		CMIP5	On-line computation				
C <sub>10</sub> H <sub>16</sub>		CMIP6	On-line computation				
CH <sub>4</sub>	CMIP6	CMIP6	MOZART2		MOZART2	CMIP6	
CO	CMIP6	CMIP6	ACCMIP	MOZART2	ACCMIP	CMIP6	
H <sub>2</sub>	MOZART2	CMIP6		MOZART2	MOZART2		
N <sub>2</sub> O	MOZART2	CMIP6		MOZART2	MOZART2		
NH <sub>3</sub>	CMIP6	CMIP6		ACCMIP	ACCMIP	CMIP6	
NO	CMIP6	CMIP6		ACCMIP		CMIP6	
SO <sub>2</sub>	CMIP6	CMIP6				CMIP6	ACCMIP
DMS					ACCMIP		
OC1	CMIP6	CMIP6				CMIP6	
OC2	CMIP6	CMIP6	On-line computation			CMIP6	
BC1	CMIP6	CMIP6				CMIP6	
BC2	CMIP6	CMIP6				CMIP6	

Table 5. Global budgets for DMS, SO<sub>2</sub>, and sulfate in the period of 1991 to 2000. Units are sources and sinks, Tg(S) yr<sup>-1</sup>; burden, Tg; lifetime, days.

		BCC-ESM (1991-2000 mean)	Other studies and CMIP5 data
DMS	Sources	27.4	
	Emission	27.4	10.7-23.7 <sup>a</sup>
	Sinks	28.0	
	Gas-phase oxidation	28.0	
	Burden	0.12	0.04-0.29 <sup>a</sup>
	Lifetime	0.78	0.5-3.0 <sup>a</sup>
SO <sub>2</sub>	Sources	76.93	
	Emission at surface	63.63	
	Emission from airplane	0.10	
	DMS oxidation	13.20	10.0-24.7 <sup>a</sup>
	Sinks	76.96	
	Dry deposition	18.53	16.0-55.0 <sup>a</sup>
	Wet deposition	9.36	0.0-19.9 <sup>a</sup>
	Gas-phase oxidation	10.33	6.1-16.8 <sup>a</sup>
	Aqueous-phase oxidation	38.74	24.5-57.8 <sup>a</sup>
Burden	0.48	0.40-1.22 <sup>a</sup>	
Lifetime	1.12	0.6-2.6 <sup>a</sup>	
SO <sub>4</sub> <sup>2-</sup>	Sources	49.05	59.67 ± 13.13 <sup>b</sup>
	Emission	0.00	
	SO <sub>2</sub> aqueous-phase oxidation	38.73	
	SO <sub>2</sub> gas-phase oxidation	10.32	
	Sinks	49.06	
	Dry deposition	2.20	4.96-5.51 <sup>d</sup>
	Wet deposition	46.86	39.34-40.20 <sup>d</sup>
	Burden	1.89	1.98 ± 0.48 <sup>b</sup> , 1.71 <sup>c</sup> , 1.2 <sup>g</sup> , 2.22-2.43 <sup>h</sup>
	Lifetime	4.69	4.12 ± 0.74 <sup>b</sup> , 3.72-3.77 <sup>d</sup> 3.3 <sup>g</sup> , 3.7-4.0 <sup>h</sup>

Notes: References denote a for Liu et al. (2005), b for Textor et al. (2006), c for the values derived from CMIP5 prescribed aerosol masses averaged from 1991 to 2000, d for Liu et al. (2012), g for Matsui and Mahowald (2017), and h for Tegen et al. (2019). Values of DMS, SO<sub>2</sub>, and sulfate burdens in the literature d are transferred from TgS to Tg (species) for units consistence.



Table 6. Same as Table 5, but for global budgets for black carbon, organic carbon, dust, and sea salts. Units are sources and sinks, Tg yr<sup>-1</sup>; burden, Tg; lifetime, days.

		BCC-ESM (1991-2000 mean)	Other studies and CMIP5 data
BC	Sources	7.22	
	Emission	7.22	11.9 ± 2.7 <sup>b</sup> , 7.8 <sup>g</sup>
	Sinks	7.24	7.75 <sup>d</sup> , 7.8 <sup>g</sup>
	Dry deposition	0.90	0.27 <sup>g</sup> , 1.30-1.64 <sup>e</sup>
	Wet deposition	6.34	7.5 <sup>g</sup> , 6.10-6.45 <sup>e</sup>
	Burden	0.13	0.114 <sup>c</sup> , 0.24 ± 0.1 <sup>b</sup> , 0.11 <sup>g</sup> , 0.14-0.26 <sup>h</sup> , 0.084-0.123 <sup>e</sup>
	Lifetime	6.60	7.12 ± 2.35 <sup>b</sup> , 3.95-4.80 <sup>e</sup> , 5.0 <sup>g</sup> , 6.3-7.5 <sup>h</sup>
OC	Sources	32.29	
	Fossil and biofuel emission	13.91	
	Natural emission	18.38	
	Sinks	32.30	
	Dry deposition	2.44	
	Wet deposition	29.86	
	Burden	0.62	0.69 <sup>c</sup> , 1.7 ± 0.45 <sup>b</sup> , 1.0-2.2 <sup>h</sup>
Lifetime	5.00	6.54 ± 1.76 <sup>b</sup> , 4.56-4.90 <sup>d</sup> , 6.4 <sup>g</sup> , 5.4-6.6 <sup>h</sup>	
Dust	Sources	2592.0	1840 <sup>b</sup> , 2943.5-3121.9 <sup>d</sup> , 2677 <sup>g</sup>
	Sinks	2592.0	
	Dry deposition	1630.8	1444 <sup>g</sup>
	Wet deposition	961.2	1245 <sup>g</sup>
	Burden	22.93	20.41 <sup>c</sup> , 22.424.7 <sup>d</sup> , 35.9 <sup>f</sup> , 19.2 ± 7.68 <sup>b</sup> , 28.5 <sup>g</sup> , 16.5-17.9 <sup>h</sup>
	Lifetime	3.23	4.14 ± 1.78 <sup>b</sup> , 2.61-3.07 <sup>d</sup> , 3.9 <sup>g</sup> , 5.3-5.7 <sup>h</sup>
Sea Salt	Sources	4667.2	4965.5-5004.1 <sup>d</sup> , 5039 <sup>g</sup>
	Sinks	4667.4	
	Dry deposition	2978.5	2158 <sup>g</sup>
	Wet deposition	1688.9	2918 <sup>g</sup>
	Burden	11.89	7.58-10.37 <sup>a</sup> , 6.4 ± 3.4 <sup>b</sup> , 11.84 <sup>c</sup> , 13.6 <sup>g</sup> , 3.9 <sup>h</sup>
	Lifetime	0.93	0.41 ± 0.24 <sup>b</sup> , 0.55-0.76 <sup>d</sup> , 0.98 <sup>g</sup> , 1.2-1.3 <sup>h</sup>

Notes: References denote a for Liu et al. (2005), b for Textor et al. (2006), c derived from CMIP5 prescribed aerosol masses averaged from 1991 to 2000, d for Liu et al. (2012), e for Liu et al. (2016), f for Ginoux (2001), g for Matsui and Mahowald (2017), and h for Tegen et al. (2019).

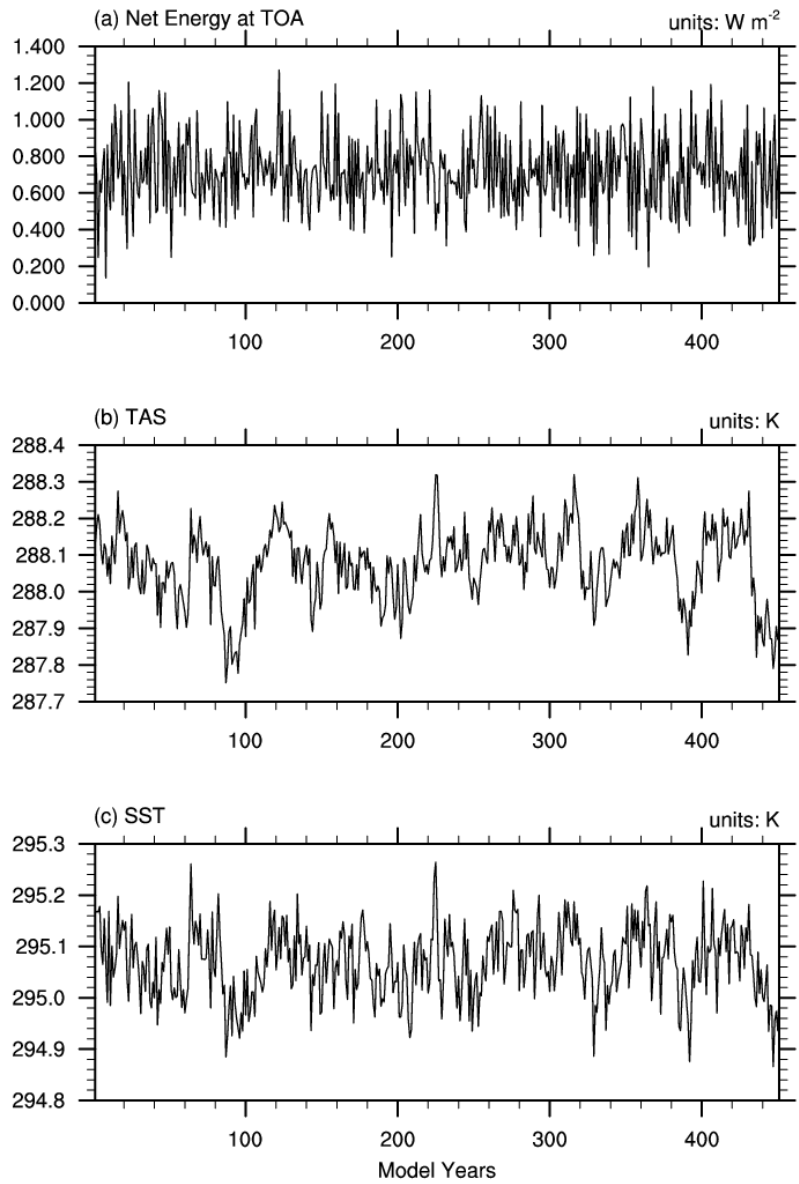


Figure 1. The time series of global and annual mean of (a) net energy budget at top of atmosphere ( $\text{W m}^{-2}$ ), (b) near-surface air temperature (K), and (c) sea surface temperature (K) in the last 450 years of the piControl simulation.

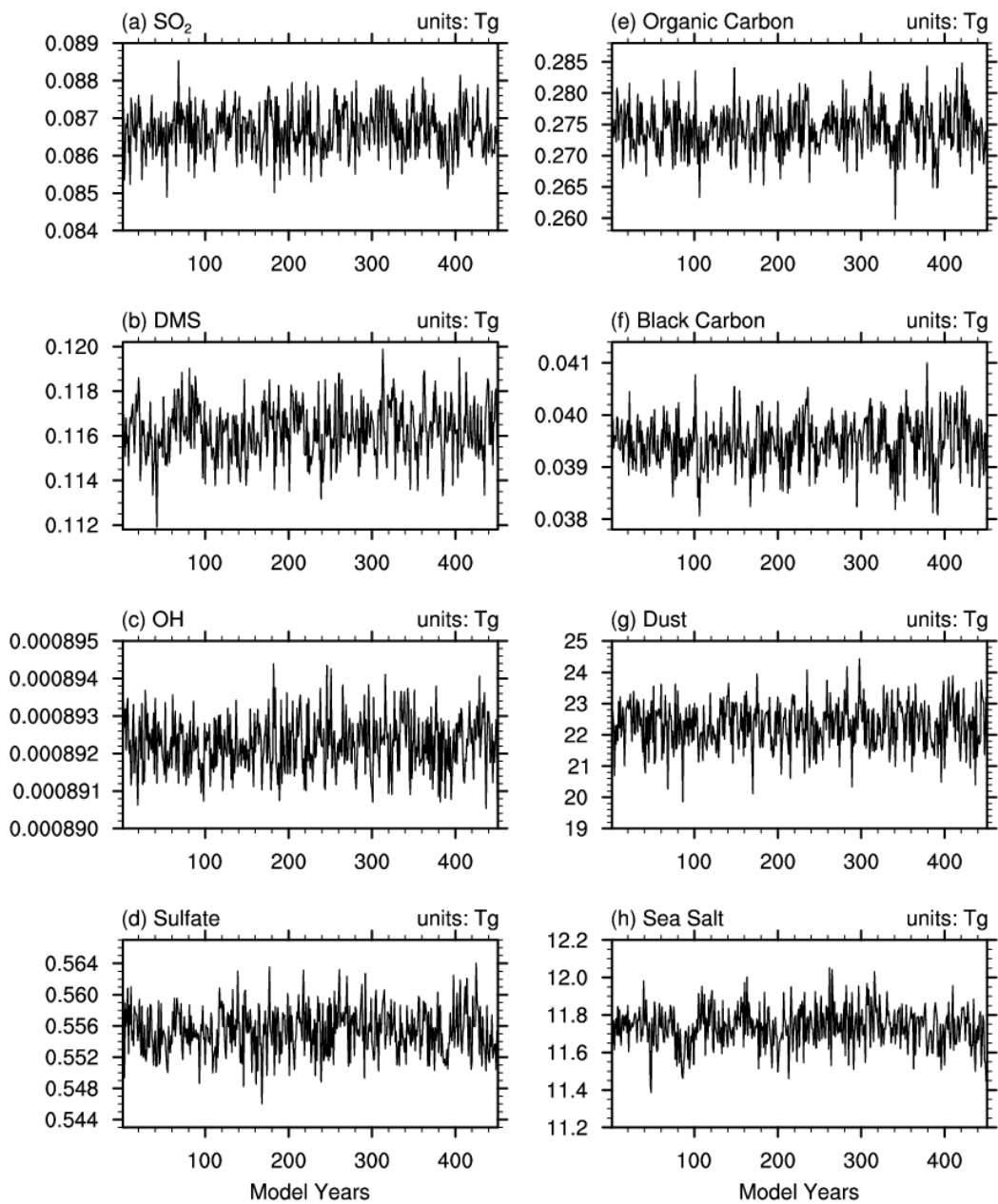


Figure 2. Same as in Figure 1, but for the global burdens of (a)  $\text{SO}_2$ , (b) DMS, (c) OH, and (d-h) different aerosols in the troposphere (below 100 hPa). Units are Tg.

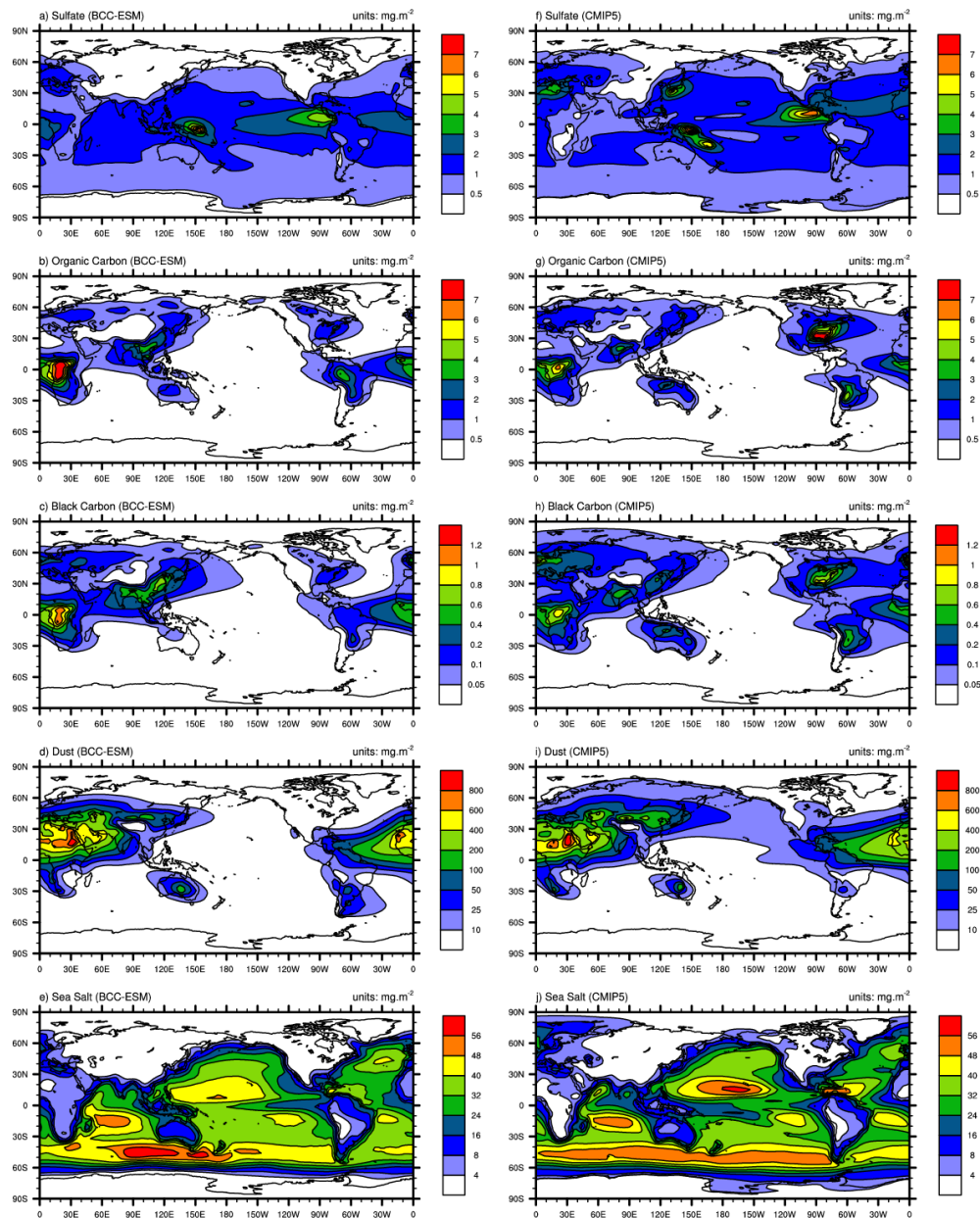


Figure 3. Global distributions of annual mean mass burdens of sulfate ( $\text{SO}_4^{2-}$ ; first row), organic carbon (OC; second row), black carbon (BC; third row), dust (fourth row), and sea salt (fifth row) aerosols in the whole atmospheric column. The left panels show the mean averaged for the last 100 years of BCC-ESM pre-industrial piControl simulations, and the right panels show the CMIP5 recommended aerosol concentrations in year 1850 (the website at IASA <http://tntcat.iiasa.ac.at/RcpDb/>). Units:  $\text{mg m}^{-2}$ .

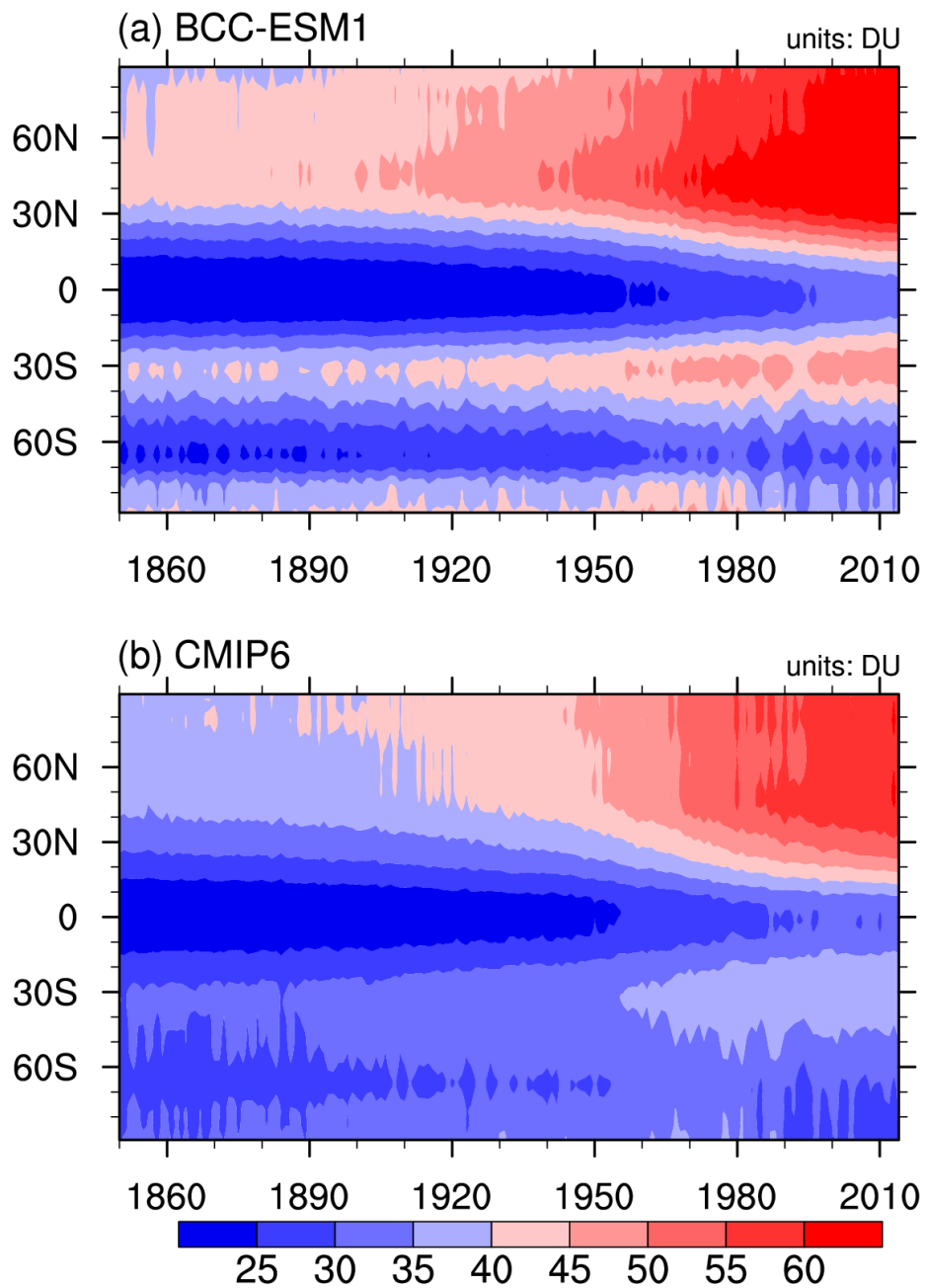


Figure 4. Zonal mean of yearly mean concentration of ozone column in the troposphere below 300 hPa to the ground from 1871 to 1999 for (a) BCC-ESM1 and (b) CMIP6 data. Unit: DU.

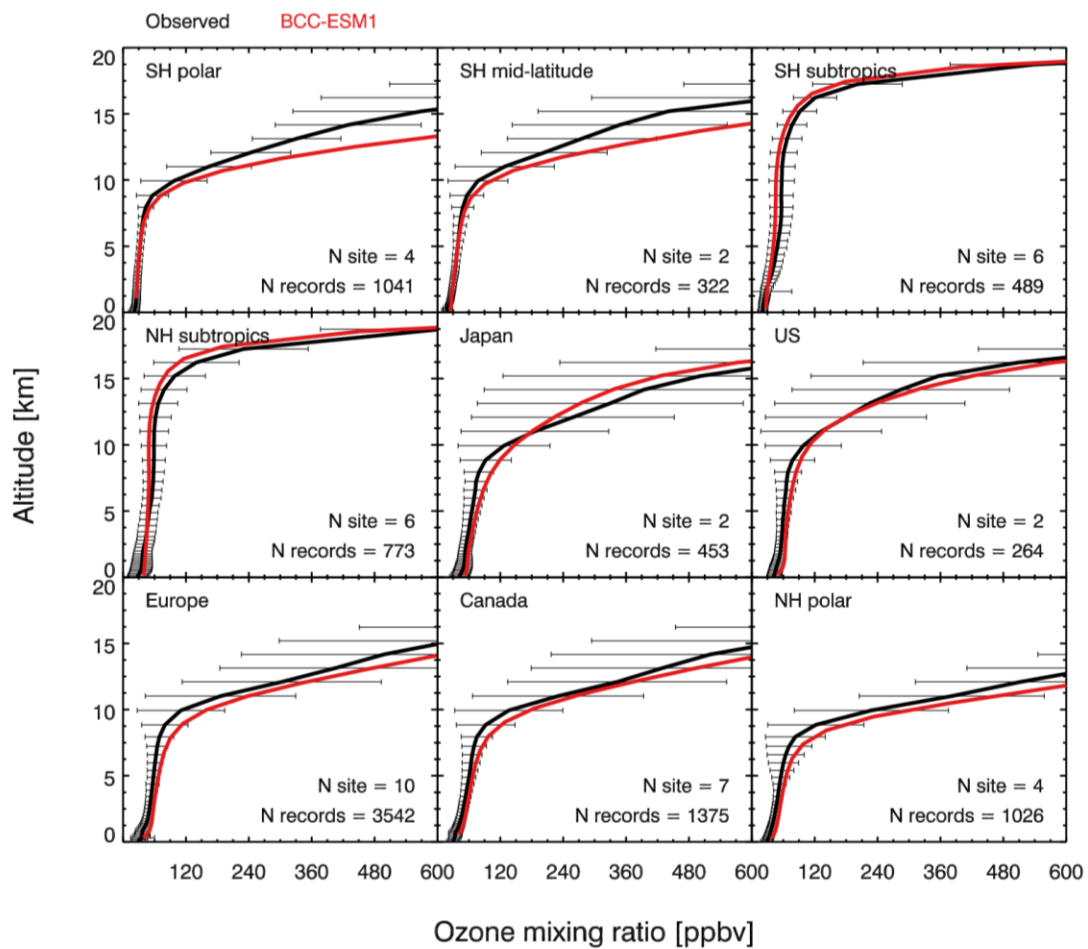


Figure 5. Vertical profiles of annual mean ozone concentrations from observations averaged for 2010-2014 in nine regions (black) and from the BCC-ESM1 simulations (red). The observations are derived from 41 global WOUDC sites.

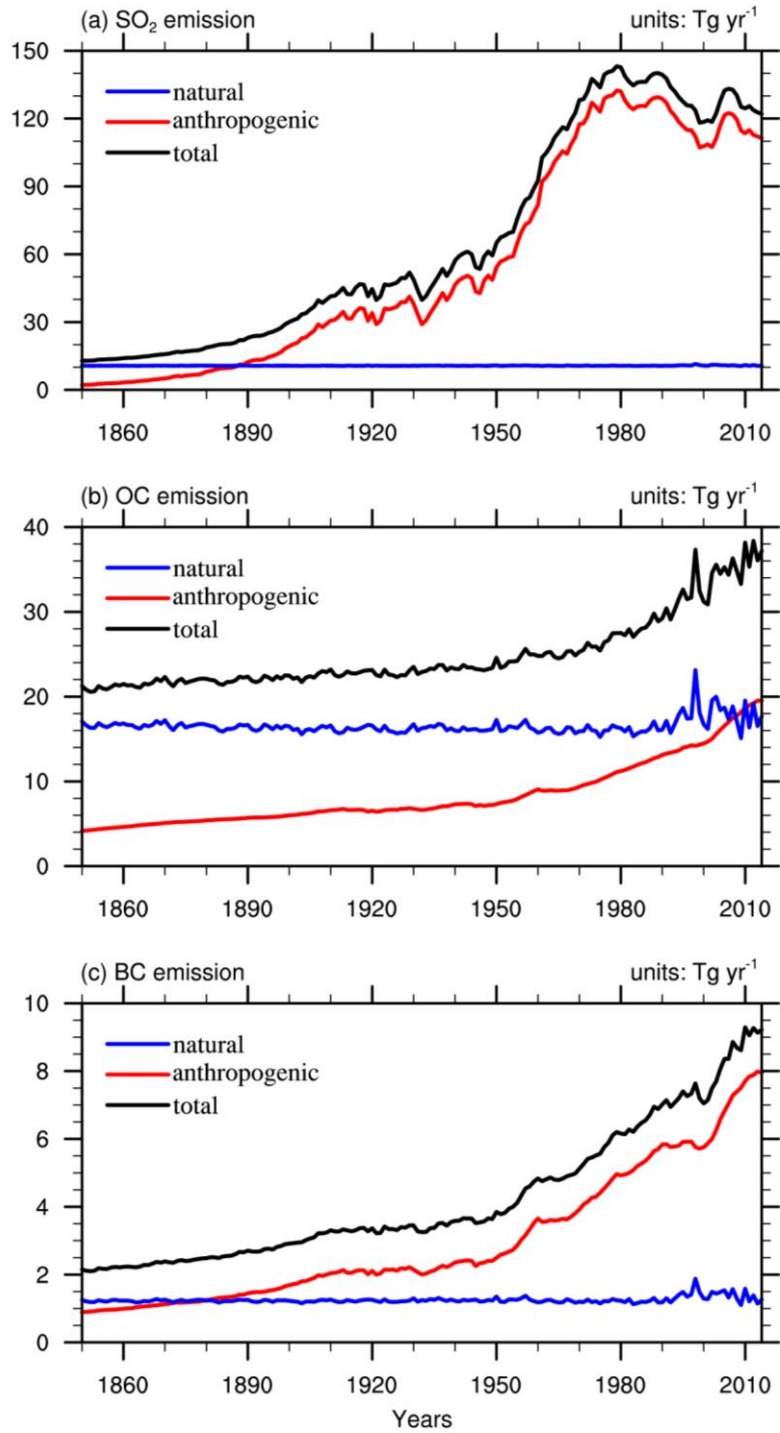


Figure 6. Global annual anthropogenic, natural, and total emissions of SO<sub>2</sub>, organic carbon (OC), and black carbon (BC) in the BCC-ESM1 historical simulation. All the biomass burning emissions are included in natural emissions in (a)-(c). Units:  $\text{Tg yr}^{-1}$ .

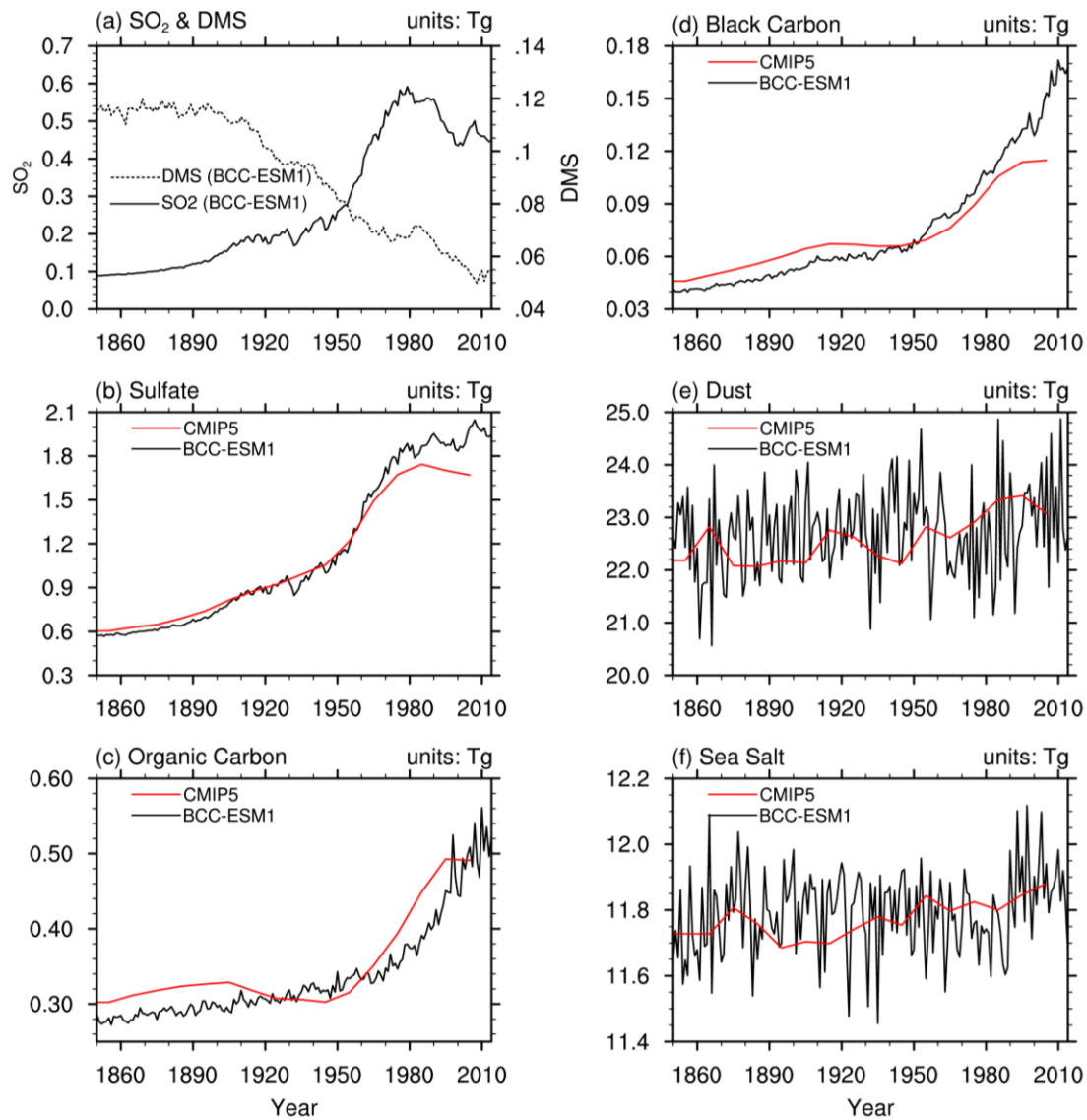


Figure 7. The time series of global yearly amounts of (a) SO<sub>2</sub> and DMS and (b-f) aerosols in the whole atmosphere column from the CMIP6 historical simulations of BCC-ESM1 (black lines) and the CMIP5-recommended aerosols masses (red lines). The yearly CMIP5 data are interpolated from the time series in 10-year interval. Units: Tg.



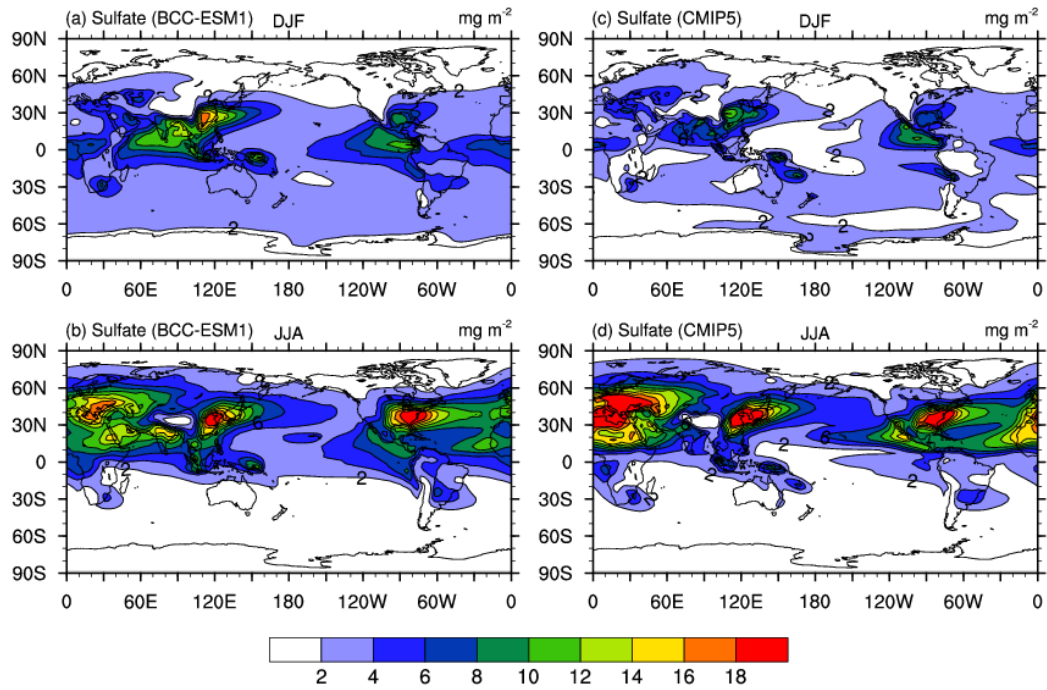


Figure 8. December-January-February (DJF; top panels) and June-July-August (JJA; bottom panels) mean sulfate ( $\text{SO}_4^{2-}$ ) aerosol column mass concentrations averaged for the period of 1971-2000. Left panels show the historical simulations of BCC-ESM1, and right panels the CMIP5-recommended data. Units:  $\text{mg}\cdot\text{m}^{-2}$ .

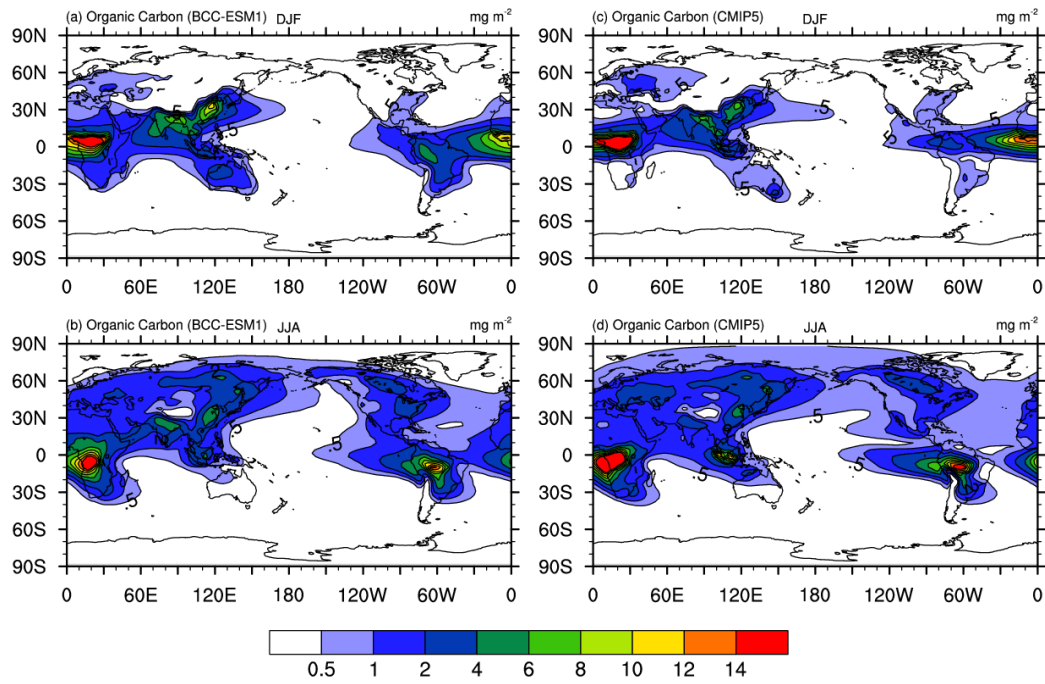


Figure 9. The same as in Figure 8, but for organic carbon (OC) aerosol column mass concentrations. Units:  $\text{mg m}^{-2}$ .

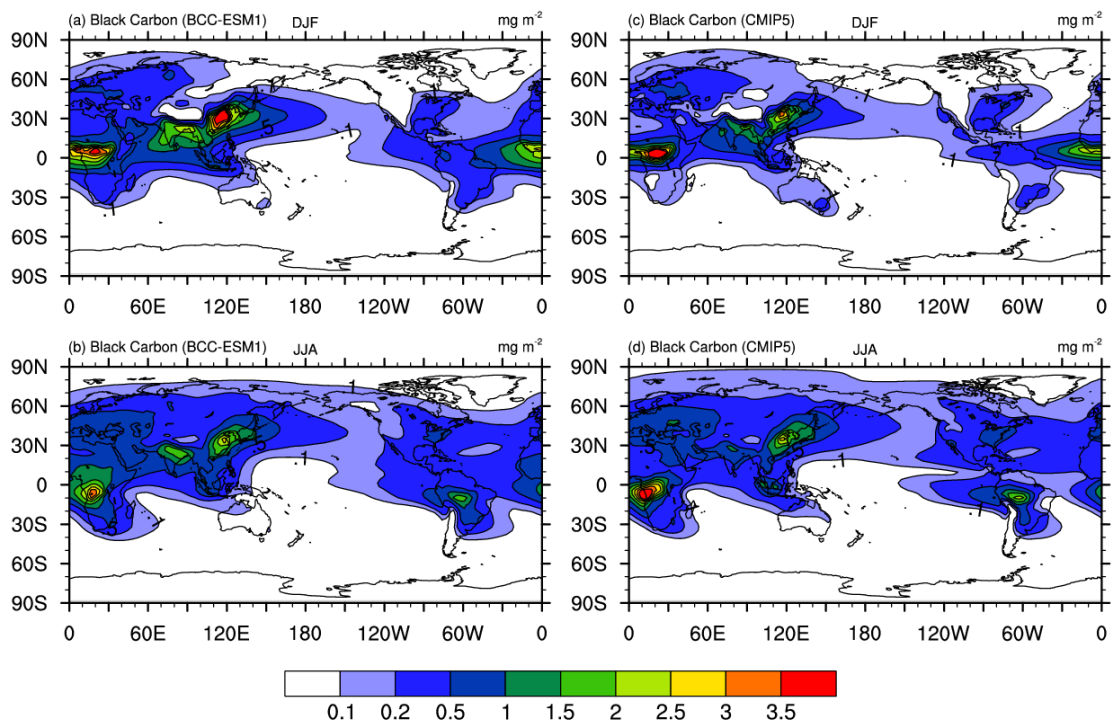


Figure 10. The same as in Figure 8, but for black carbon (BC) aerosol. Units:  $\text{mg.m}^{-2}$ .

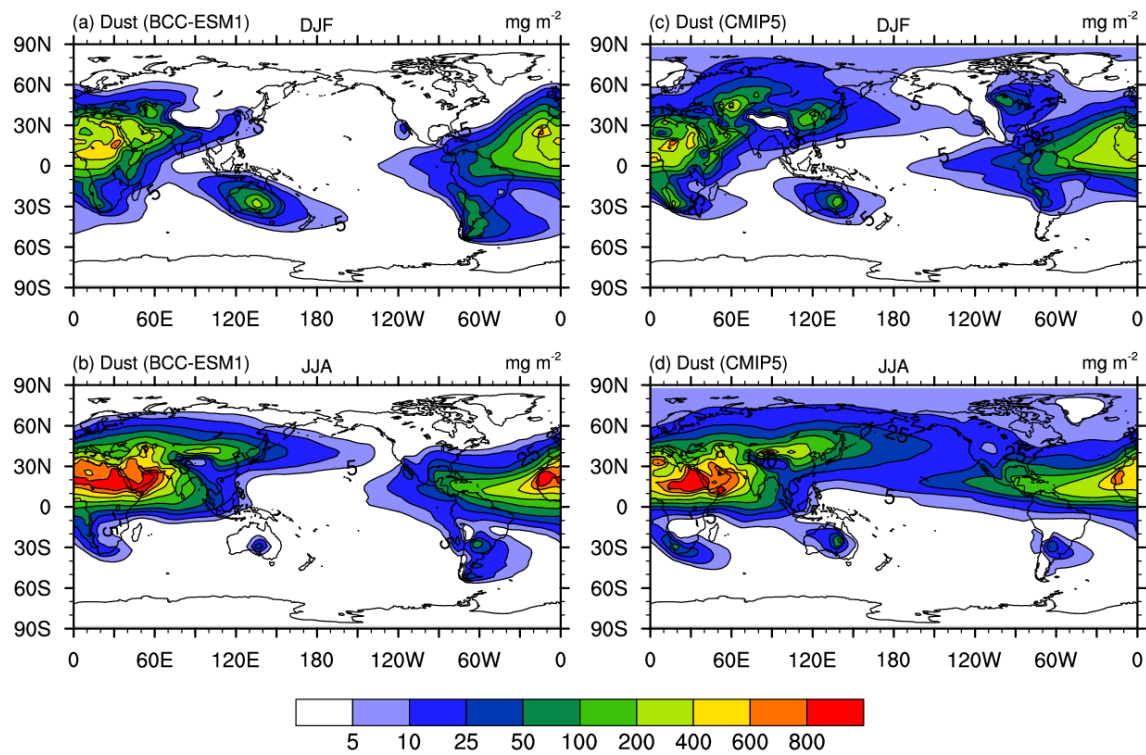


Figure 11. The same as in Figure 8, but for dust aerosol. Units:  $\text{mg.m}^{-2}$ .

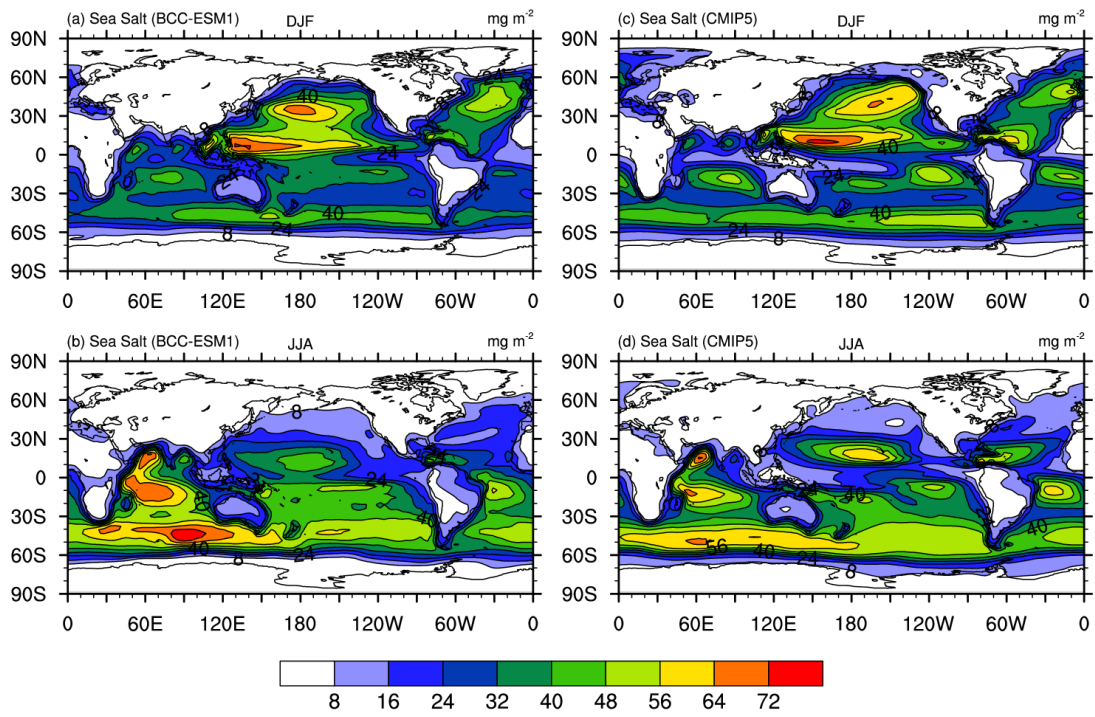


Figure 12. The same as in Figure 8, but for sea salt (SSLT) aerosol. Units:  $\text{mg.m}^{-2}$ .

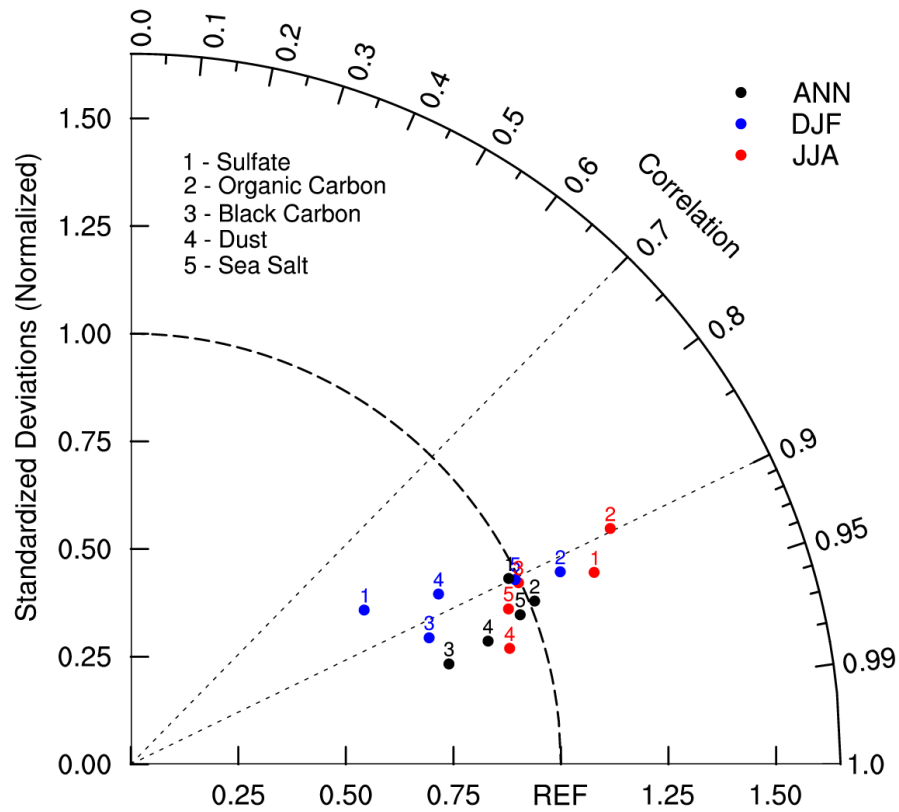


Figure 13. Taylor diagram for the global aerosols climatology (1971–2000) of sulfate, organic carbon, black carbon, dust, and sea salt averaged for December-January-February (DJF), June-July-August (JJA), and annual respectively. The radial coordinate shows the standard deviation of the spatial pattern, normalized by the observed standard deviation. The azimuthal variable shows the correlation of the modelled spatial pattern with the observed spatial pattern. Analysis is for the whole globe. The reference dataset is CMIP5-prescribed dataset.

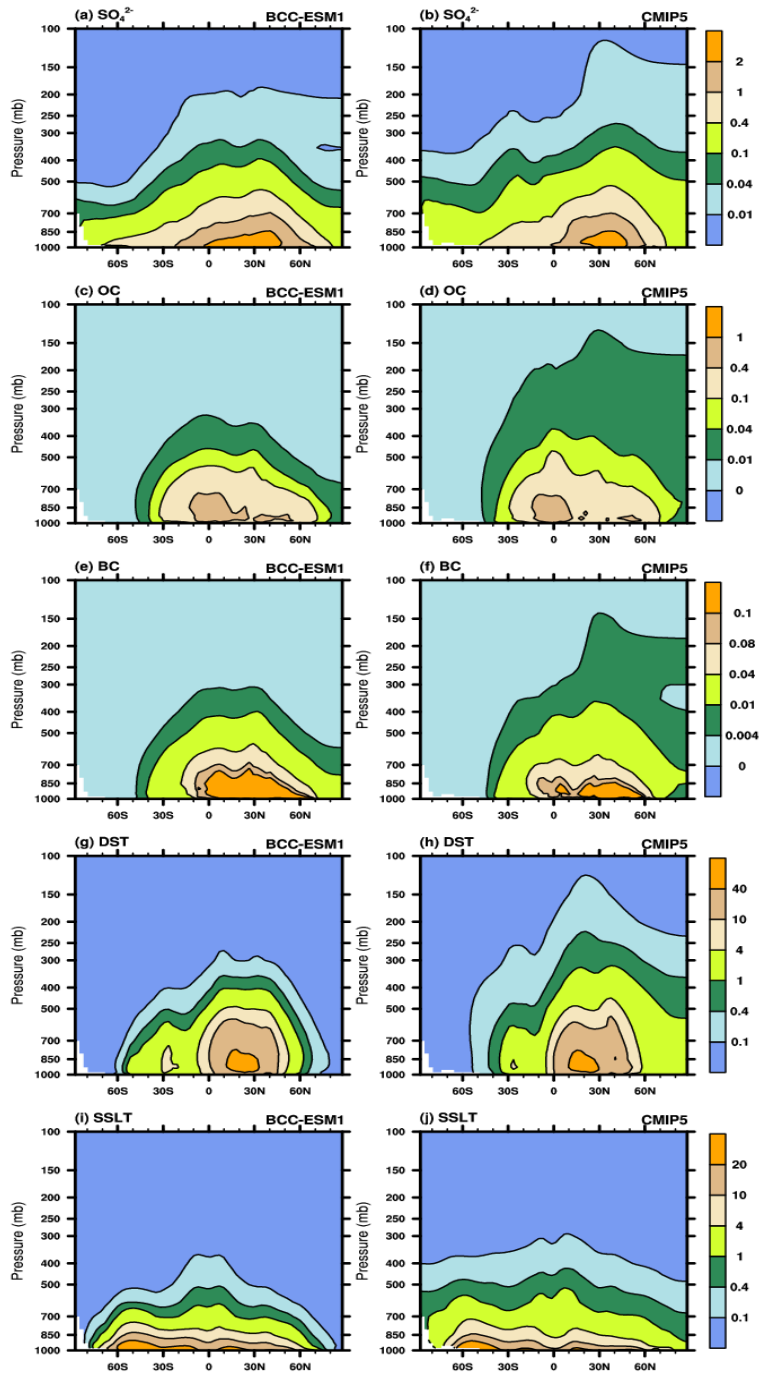


Figure 14. Latitude-pressure distributions of zonally-averaged annual mean sulfate, organic carbon, black carbon, dust, and sea salt aerosol concentrations for the period of 1971-2000. Left panels show the CMIP6 historical simulation of BCC-ESM1, and right panels the CMIP5 recommendation data. Units:  $\mu\text{g m}^{-3}$ .

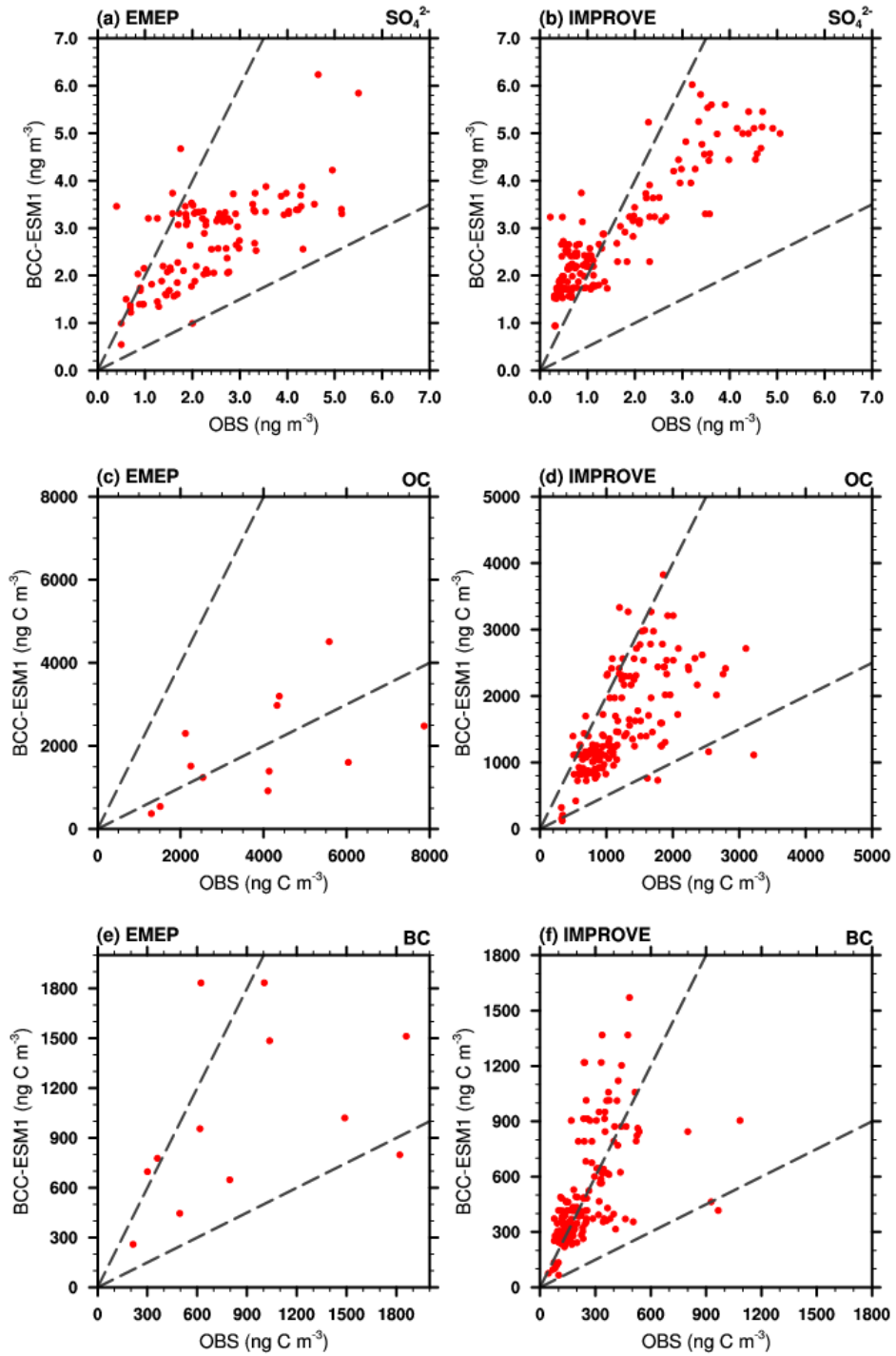


Figure 15. Scatter plots showing observed versus simulated multi-years averaged annual mean sulfate ( $\text{SO}_4^{2-}$ ), organic carbon (OC), black carbon (BC) mixing ratios at IMPROVE and EMEP network sites. Observations are averages over the available years 1990–2005 for IMPROVE sites, and 1995–2005 for EMEP sites. Simulated values are those at the lowest layer of BCC-ESM1.



Table 7. Observed versus simulated concentrations of sulfate ( $\text{SO}_4^{2-}$ ), organic carbon (OC), black carbon (BC) for the regional mean and spatial standard deviation, minimum and maximum values at IMPROVE and EMEP network sites, and the spatial correlation between observed and simulated multi-years averaged annual means. Simulated values are selected for the same locations and same valid observation time. The data used same as those in Figure 12.

	EMEP			IMPROVE		
	$\text{SO}_4^{2-}$ (Obs/Model)	OC (OBS/Model)	BC (OBS/Model)	$\text{SO}_4^{2-}$ (OBS/Model)	OC (OBS/Model)	BC (OBS/Model)
<b>Mean Values</b>	2.37/2.74	3844/1919	884/1022	1.53/2.79	1215/1565	249/504
<b>Std Deviation</b>	1.16/0.93	1997/1215	572/526	1.30/1.20	572/745	164/296
<b>Min Values</b>	0.40/0.55	1296/369	214/259	0.22/0.94	322/123	45/66
<b>Max Values</b>	5.50/6.24	7867/4510	1859/1834	5.07/6.02	3219/3827	1084/1570
<b>Correlation (Obs and Model)</b>	0.67	0.56	0.40	0.90	0.63	0.55

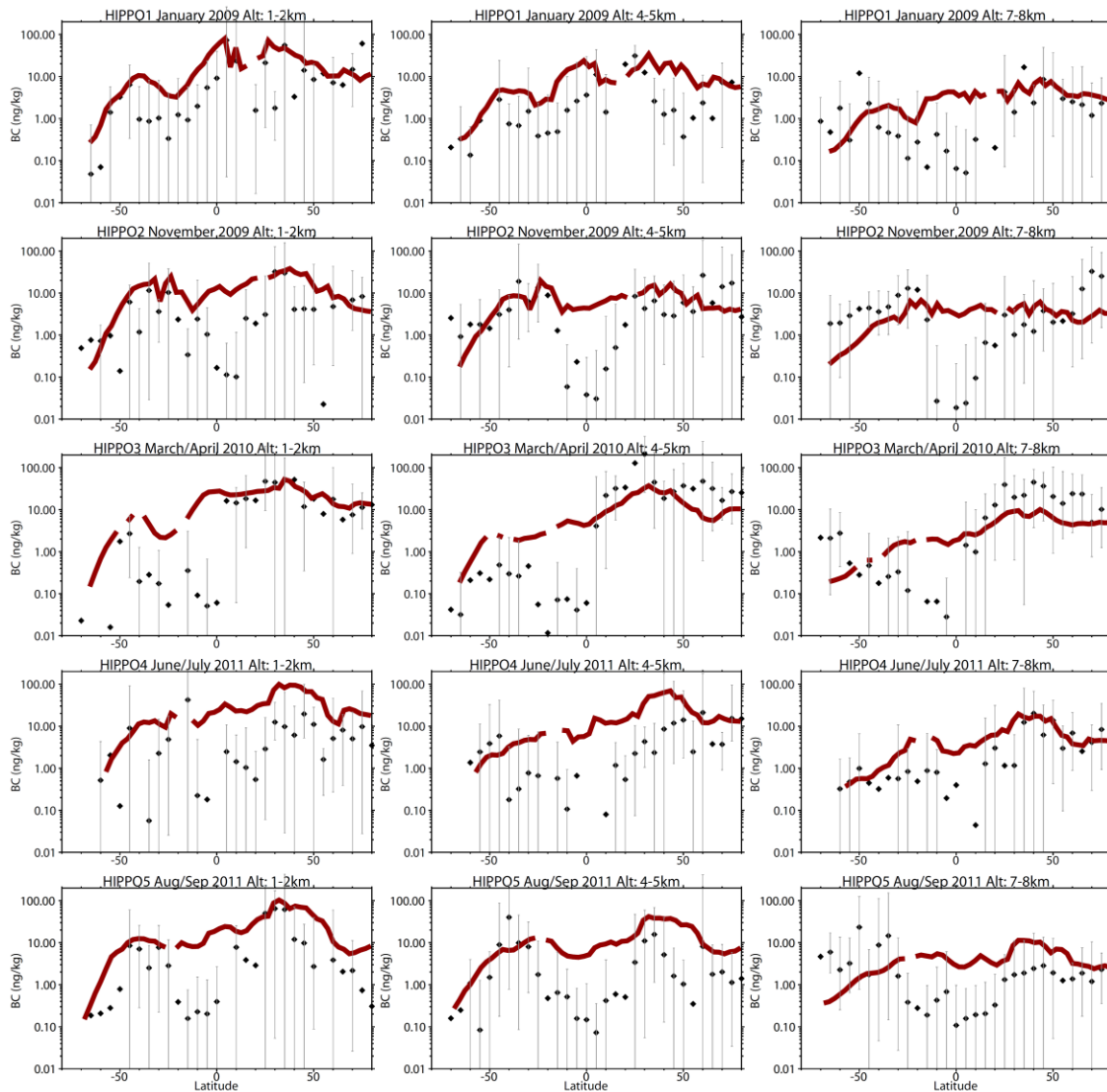


Figure 16. Comparison of modelled black carbon (BC) aerosol (red lines) with observations from HIPPO aircraft campaigns over the Pacific Ocean (black symbols, bars represent the full data range). Observations from different HIPPO campaigns were averaged over  $5^\circ$  latitude bins and three different altitude bands (left column: 1-2 km, middle column: 4-5 km, and right column: 7-8 km) along the flight track over the Pacific Ocean. Model results were sampled along the flight track and then averaged over the abovementioned regions for comparison.

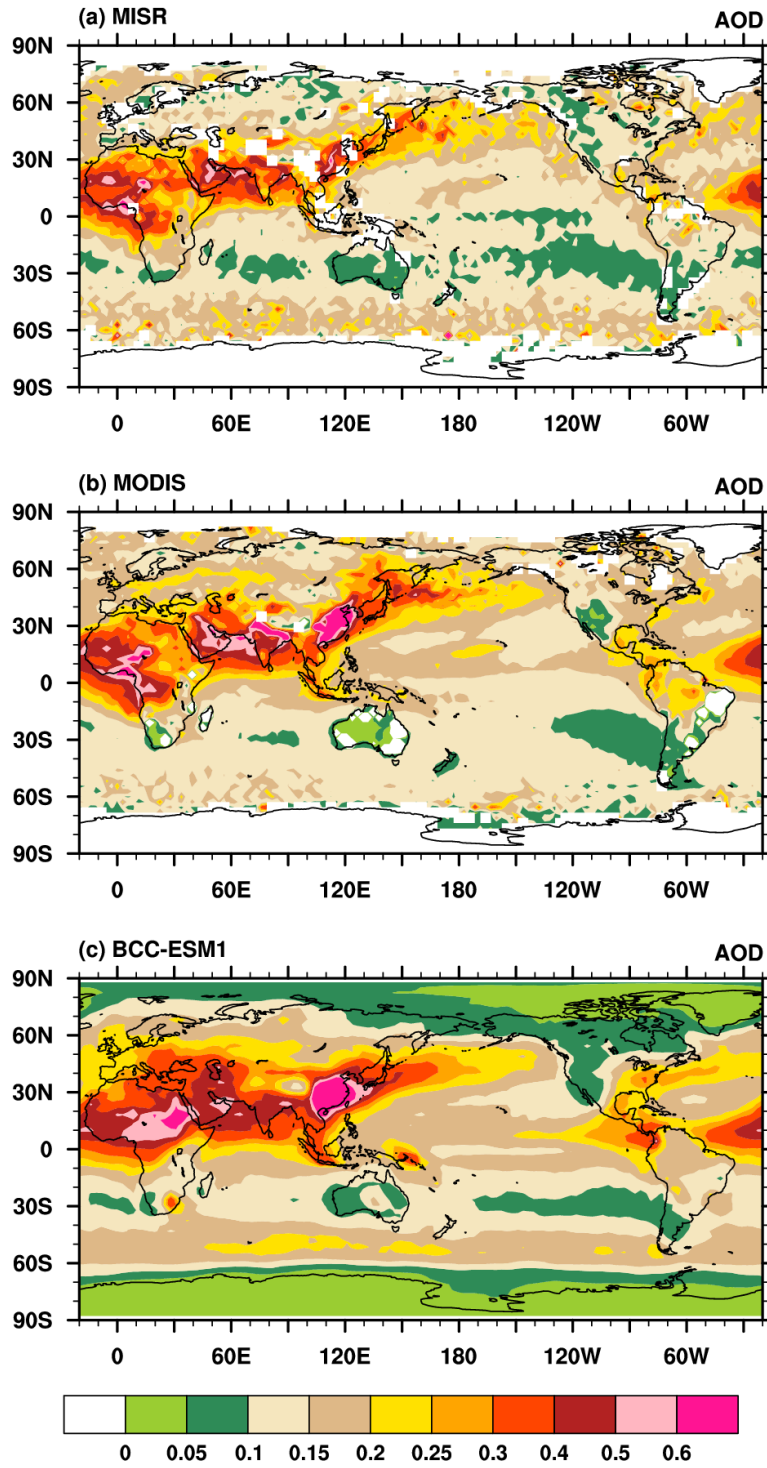


Figure 17. Global distribution of annual mean AOD simulated in BCC-ESM1 compared with the MISR and MODIS data for the year 2008.

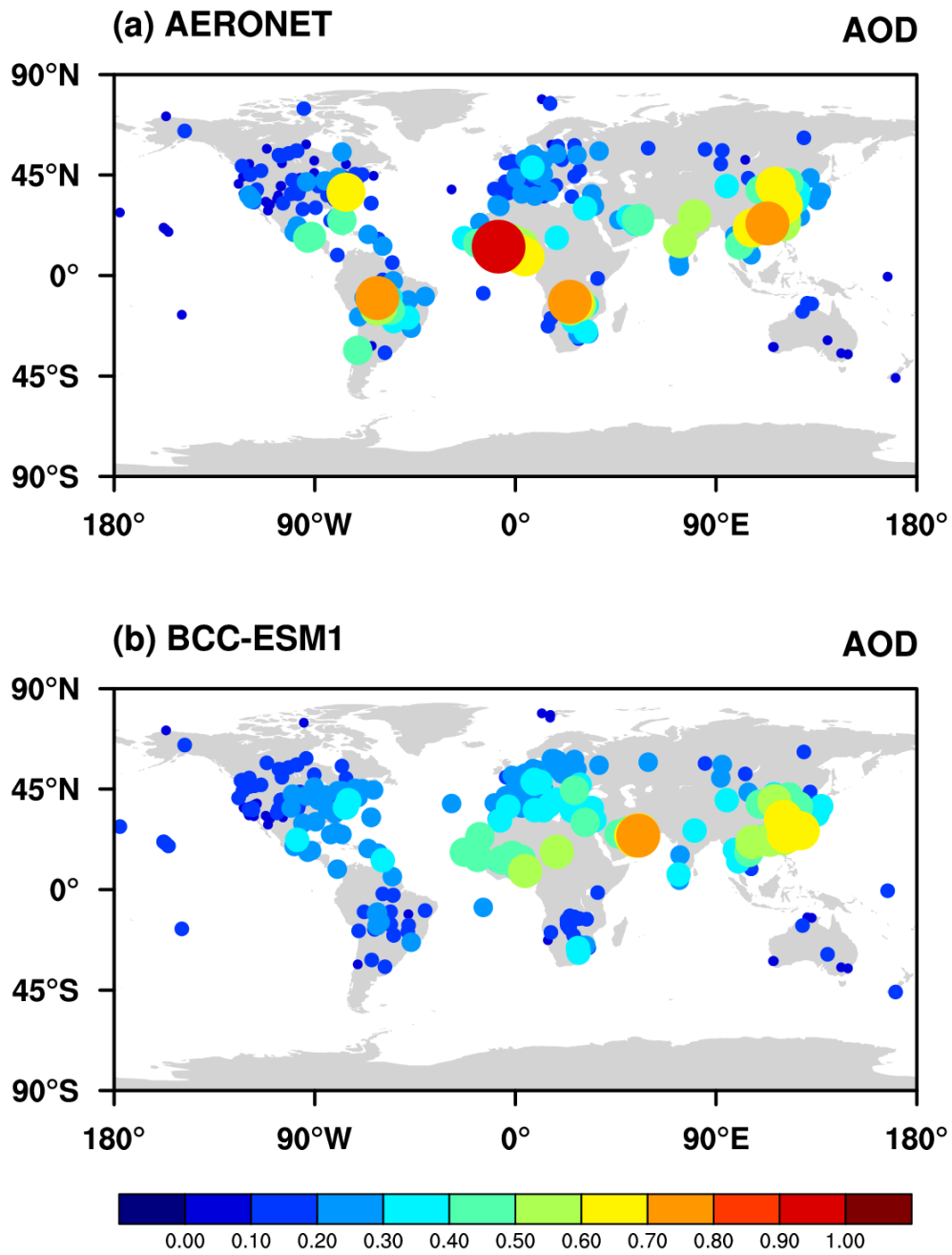


Figure 18. Observed versus simulated annual means of AOD at AERONET sites. Each data point represents the mean averaged for available monthly values of AOD. The dot sizes denote the magnitudes of AOD at sites. The spatial correlation is 0.56.

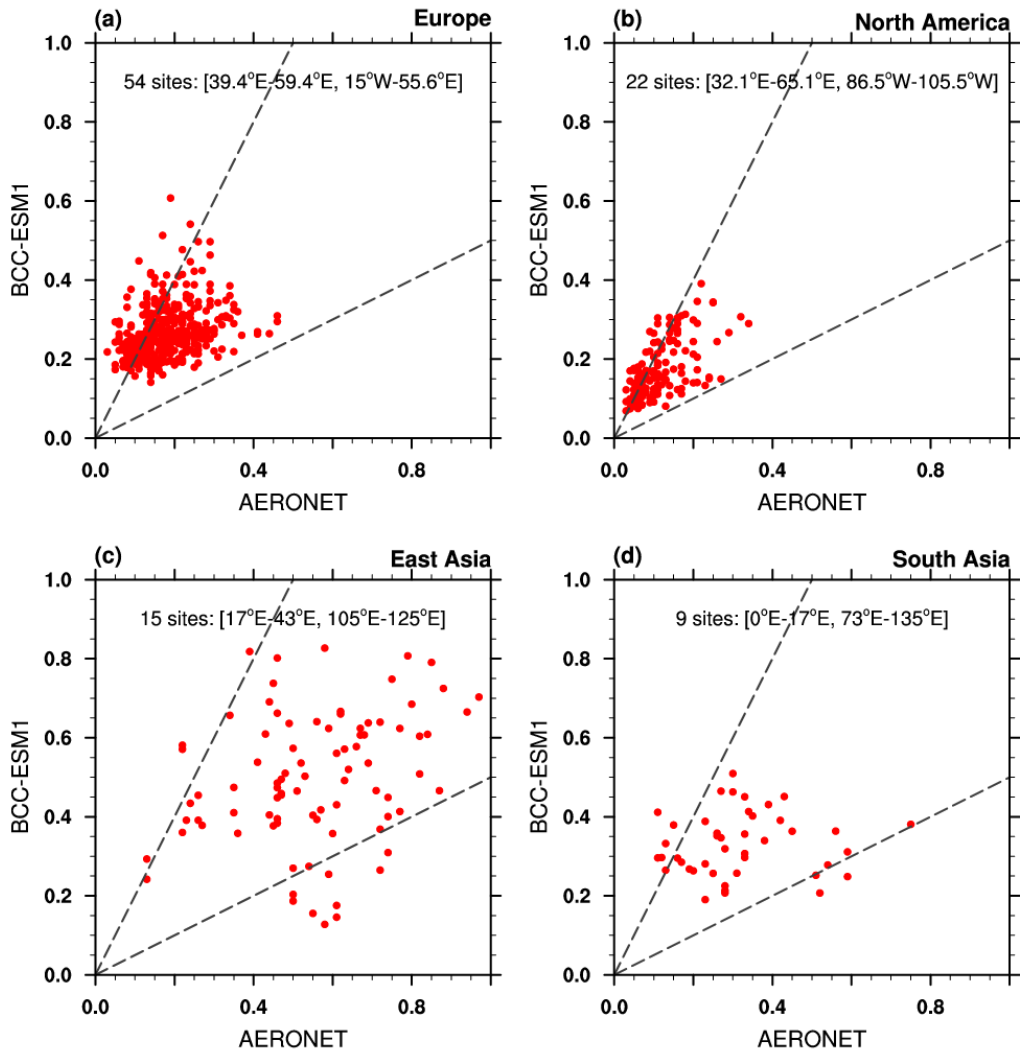


Figure 19. Scatter plots of observed versus simulated monthly mean AOD at AERONET sites in Europe, North America, East Asia, and South Asia over the period of 1998-2005.